

Search for Higgs Decay to Dark Matter and Trigger Studies

João Carlos Arnauth Pela
of Imperial College London

A dissertation submitted to Imperial College London
for the degree of Doctor of Philosophy

The copyright of this thesis rests with the author and is made available under a Creative Commons Attribution Non-Commercial No Derivatives licence. Researchers are free to copy, distribute or transmit the thesis on the condition that they attribute it, that they do not use it for commercial purposes and that they do not alter, transform or build upon it. For any reuse or redistribution, researchers must make clear to others the licence terms of this work.

Abstract

Here the abstract of the thesis

Declaration

This dissertation is the result of my own work, except where explicit reference is made to the work of others, and has not been submitted for another qualification to this or any other university. This dissertation does not exceed the word limit for the respective Degree Committee.

João Pela

Acknowledgements

TODO:

- Family
- Friends
- Work colleagues (include CMS collaboration)
- more

The work presented in this thesis was supported by the Portuguese Government through **Fundaçao para a Ciéncia e a Tecnologia (FCT)** in the form of my PhD grant with the reference SFRH/BD/77979/2011. I am thankful for their support which allowed me to attain higher education.



Preface

Thesis structure and so on...

“To my grand mother”

Contents

1 Experimental Apparatus	2
1.1 The Large Hadron Collider	2
1.1.1 Running and performance	5
1.2 The Compact Muon Solenoid Experiment	8
1.2.1 Geometry and conventions	9
1.2.2 Inner tracking system	10
1.2.3 Electromagnetic Calorimeter	11
1.2.4 Hadronic Calorimeter	13
1.2.5 Solenoid Magnet	15
1.2.6 Muon System	15
1.2.7 Data Acquisition System	18
1.2.8 Trigger System	18
1.2.9 Computing	20
1.2.10 Level 1 Trigger: Stage I Upgrade	21
2 Technical work	22
2.1 Data Quality Monitoring	22
2.1.1 Online Monitoring	23
2.1.2 Offline Monitoring	23
2.2 Level 1 Trigger Data Quality Monitoring	23
2.2.1 Rates Monitoring	24
2.2.2 Synchronization Monitoring	25
2.2.3 BPTX Monitoring	27
2.2.4 Occupancy Monitoring	29
2.3 Tests Summary	34
3 Event Reconstruction and simulation	36
3.1 Tracks	36
3.2 Vertex Reconstruction	37

3.3	Particle Flow	39
3.3.1	Isolation	40
3.4	Electrons	40
3.4.1	Isolation	43
3.4.2	Veto electrons	43
3.4.3	Tight electrons	43
3.5	Muons	44
3.5.1	Isolation	45
3.5.2	Loose Muons	46
3.5.3	Tight Muons	46
3.6	Jets	46
3.6.1	Jet Clustering	47
3.6.2	Particle Flow Jet Identification	48
3.6.3	Pileup Jet Identification	48
3.6.4	Lepton cleaning	49
3.6.5	Jet Energy Corrections	49
3.7	Hadronic Taus	50
3.7.1	Hadron Plus Stips Algorithm	51
3.7.2	Isolation and Discriminants	52
3.8	Missing Transverse Energy	53
3.9	Monte Carlo Simulation	54
4	Search for H(Inv) decays in the VBF channel with CMS prompt data	57
4.1	Event Selection	58
4.2	Background Estimation	60
4.3	Sources of uncertainty	64
4.4	Results and conclusions	64
Bibliography		68
List of Figures		76
List of Tables		79
Acronyms		80

Chapter 1

Experimental Apparatus

1.1 The Large Hadron Collider

The **Large Hadron Collider (LHC)** [1, 2] is currently the world's largest particle accelerator and is capable of producing the highest energy particle beams ever made by mankind. This machine has total perimeter of 26.7 km and was built at **European Organization for Nuclear Research (CERN)** in a circular tunnel, which previously housed the **Large Electron Positron collider (LEP)** [3], at an average depth of 100 m below ground under the Franco-Swiss border near Geneva, Switzerland. A diagram of the **LHC** tunnel and its experiments can be found at figure 1.1.

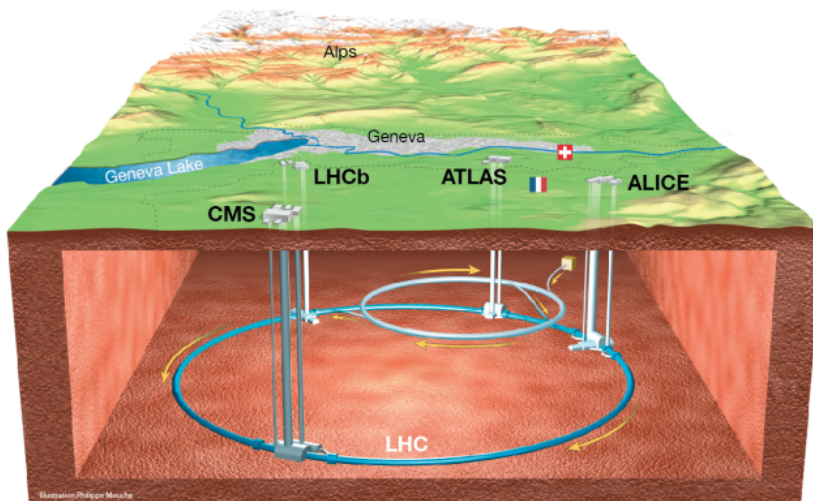


Figure 1.1: Underground diagram of the Geneva area showing the **LHC** and its experiments location [4].

The **LHC** is a synchrotron machine with the capability of accelerating two particles beams in opposite directions in two separated beam pipes. These beams only cross and are forced to collide in four points of the accelerator where particle detectors are installed to observe the products of such collisions. This experiments are: **A Toroidal LHC ApparatuS (ATLAS)** [5], **Compact Muon Solenoid (CMS)** [6], **Large Hadron Collider beauty (LHCb)** [7] and **A Large Ion Collider Experiment (ALICE)** [8].

The objective of the **LHC** program is to investigate physics at the TeV scale, more specifically to understand the electroweak symmetry breaking and if this phenomena could be explained by the Higgs mechanism. There are many **Beyond the Standard Model (BSM)** models that predict new physics at this energy regime making the **LHC** the perfect machine to investigate such phenomena. **ATLAS** and **CMS** are general-purpose detectors which aim to investigate a broad spectrum of physics. The **LHCb** detector is used to study processes that involve the decay of b-flavoured hadrons. The **ALICE** detector is optimised to look at heavy-ion collisions and to investigate the properties of extreme high density medium that is formed.

The **LHC** is only the last element of a complex accelerator chain which step-by-step increases the energy of the particles to eventually be collided [2]. Protons are initially obtained by stripping the electrons of hydrogen gas. This process happens at the beginning of the **Linear Particle Accelerator 2 (LINAC2)** which then accelerates them up to the energy of 50 MeV. After this initial step proton are injected into the **Proton Synchrotron Booster (PSB)** and the energy ramps up to 1.4 GeV. Particles are then passed to the **Proton Synchrotron (PS)** where the energy further increases to 25 GeV. Subsequently they are injected into the **Super Proton Synchrotron (SPS)** where the particle energy level reaches 450 GeV. Finally, protons pass to the **LHC** where they can be accelerated to a maximum energy of 7 TeV. A simplified diagram of the **CERN** accelerator chain can be found in figure 1.2. Normal operation of the **LHC** therefore depends on all the upstream accelerators availability. The typically turn around time, the time necessary to stop the accelerator from running and restart collisions, is around 2 hours. When stable beams are achieved, a single proton fill can be used to collide protons up to 24 hours, but it is common to restart more frequently to profit from the higher collision rates possible right at the beginning of a new fill.

Each beam pipe can be filled with proton or heavy ions. Three modes of operation have been tried: proton-proton, proton-lead ion and lead ion-lead ion. By changing the incoming particles we are changing the quantity of nucleons present at each interaction. The maximum design energy per proton is 7 TeV and is 2.76 TeV for each lead nucleon.

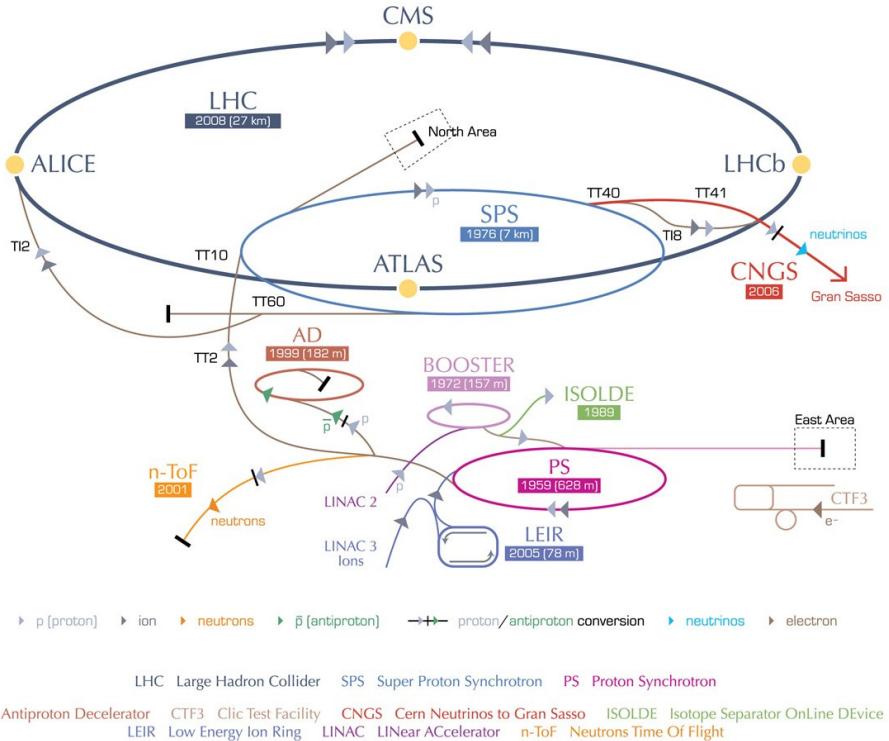


Figure 1.2: Diagram of the CERN accelerator complex [9].

The maximum design luminosity for proton-proton is $10^{34} \text{ cm}^{-2}\text{s}^{-1}$ and $10^{27} \text{ cm}^{-2}\text{s}^{-1}$ for lead ion-lead ion collisions.

Particles beams trajectory are curved by 1232 niobium-titanium superconducting dipole magnets each with a length of 14.3 m. They are cooled with superfluid helium to 1.9 K and produce the necessary magnetic field of 8.4 T. Eight Radio Frequency (RF) cavities located at the LHC point 4 are used to accelerate the beams. At each turn particle energy is increased to compensate for synchrotron radiation loss and increase the momentum. At nominal operation the LHC will steer 2808 bunches composed up to 10^{11} protons separated by 25 ns in each direction. Some of the key parameters of the LHC proton-proton and lead-lead operation can be found in table 1.1.

At the LHC we are looking for extremely rare processes. As is can be seen in figure 1.3 the production cross section of a Standard Model (SM) Higgs boson is more than 9 orders of magnitude smaller than the total proton-proton cross section.

	<i>pp</i>	HI		
Energy per nucleon	E	7	2.76	TeV
Dipole field at 7 TeV	B	8.33	8.33	T
Design Luminosity*	\mathcal{L}	10^{34}	10^{27}	$\text{cm}^{-2}\text{s}^{-1}$
Bunch separation		25	100	ns
No. of bunches	k_B	2808	592	
No. particles per bunch	N_p	1.15×10^{11}	7.0×10^7	
Collisions				
β -value at IP	β^*	0.55	0.5	m
RMS beam radius at IP	σ^*	16.7	15.9	μm
Luminosity lifetime	τ_L	15	6	h
Number of collisions/crossing	n_c	≈ 20	-	

* For heavy-ion (HI) operation the design luminosity for Pb-Pb collisions is given.

Table 1.1: The machine parameters relevant for the LHC detectors.[10]

To be able to record and study such rare processes we need to produce a significant number of collisions. For this purpose the **LHC** was designed to operate at high instantaneous luminosity, L. This quantity is defined as,

$$L = \frac{N_b^2 n_b f_{\text{rev}} \gamma}{4\pi \epsilon_n \beta^*} F, \quad (1.1)$$

where N_b is the number of protons per bunch, n_b is the number of bunches, f_{rev} is the frequency of revolution, γ is the Lorentz factor, ϵ_n is the normalized emittance, β^* is the beta function at the collision point and F is the reduction factor due to the crossing angle.

1.1.1 Running and performance

Operation of the **LHC** has started when the first beams circulated in the machine in September 2008. Unfortunately, only a few days after a faulty weld between two dipole magnets caused a significant magnet quench which in turn damaged several dipoles and a simultaneous leak of a significant amount of helium happened. The event showed that

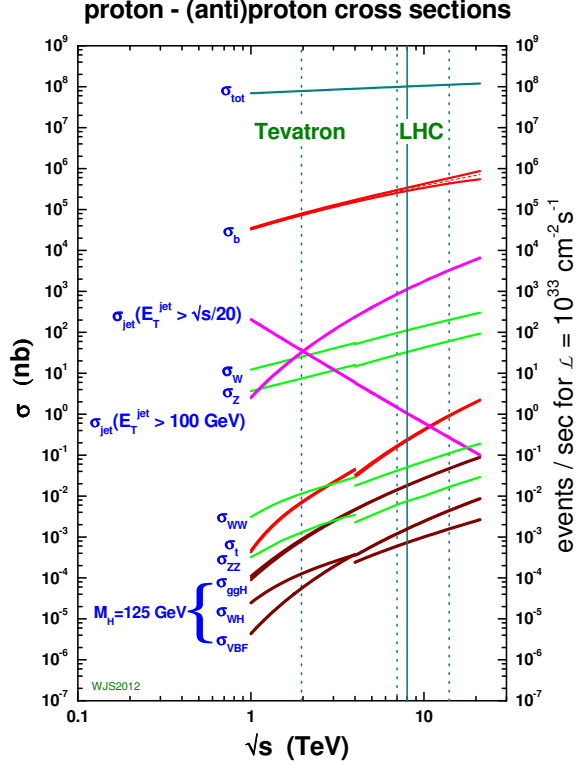


Figure 1.3: Cross sections for several processes for collisions of antiproton-proton and proton-proton as a function of the center of mass energy [6].

beyond the repair of the affected systems the accelerator needed a significant consolidation program to allow it to return to activity [11]. This consolidation program took over one year to finalise and to prevent further possible problems and allow better understanding of the machine while maximizing physics reach, it was decided to initially run the **LHC** at 7 TeV center-of-mass energy. First collisions happened at November 2009 just at the **SPS** injection energy of 450 GeV giving start to the **LHC** run I.

The collision energy was finally ramped up to 7 TeV with first collisions being observed during March 2010. Operation at this energy continued until the end of 2011, with a peak luminosity being achieved of $3.7 \times 10^{33} \text{ cm}^{-2} \text{ s}^{-1}$. The total integrated luminosity delivered to **CMS** was 6.1 fb^{-1} with the total actually recorded being 5.6 fb^{-1} . During 2012 with the increase knowledge of the accelerator it was possible to increase the centre-of-mass energy further to 8 TeV and eventually reaching peak luminosity of $7.7 \times 10^{33} \text{ cm}^{-2} \text{ s}^{-2}$ and delivering integrated luminosity of 23.3 fb^{-1} to **CMS** of which 21.79 fb^{-1} were recorded. Figure 1.4 shows the delivered luminosity in the period 2010-2013 over time.

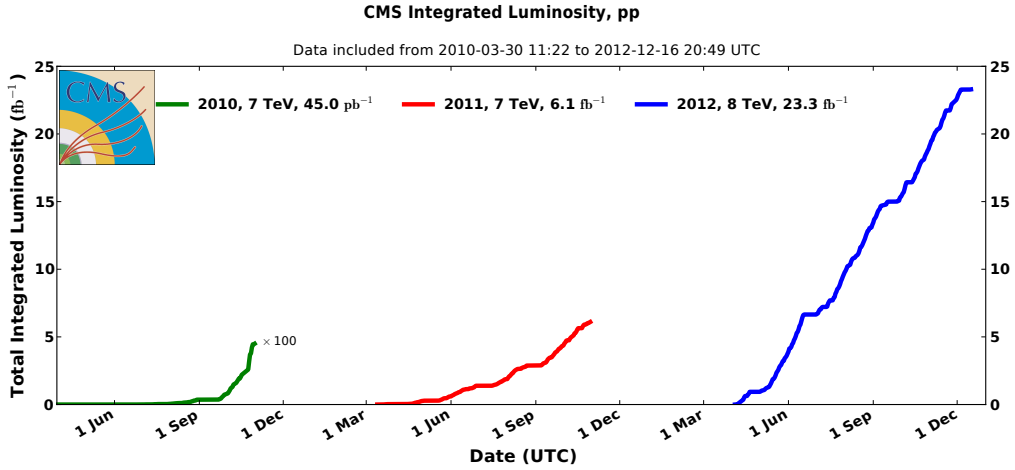


Figure 1.4: Cumulative luminosity versus day delivered to CMS during stable beams and for p-p collisions. This is shown for 2010 (green), 2011 (red) and 2012 (blue) data-taking [12].

For physics usage, data needs to undergo a certification process. In this process specialists from each CMS subsystem check that no problem has happened during data taking that would bias or invalidate the recorded events. For 2011 a total of 5.1 fb^{-1} and for 2012 a total 19.7 fb^{-1} were considered of good quality for physics.

In order to achieve high integrated luminosity LHC collides particle bunches up to 40 million times a second, and many interactions may happen simultaneously, this effect is called **Pile-Up (PU)**. Figure 1.5 shows the distribution of the mean number of interaction per bunch crossing during 2012 at the CMS experiment.

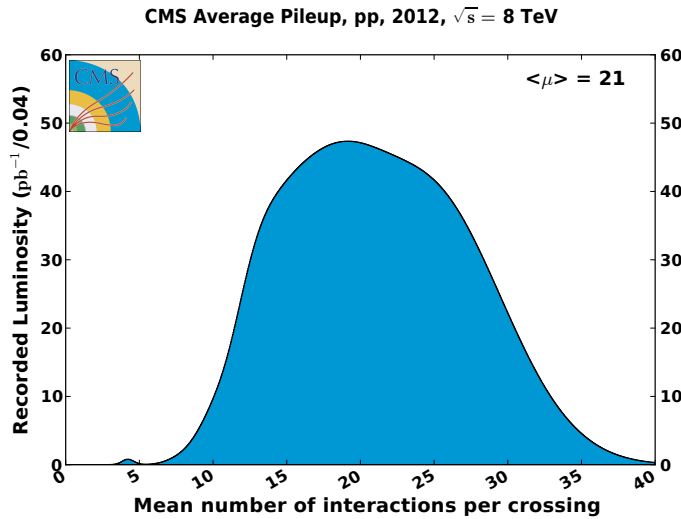


Figure 1.5: Mean number of interactions per bunch crossing at the CMS experiment during 2012 [13].

1.2 The Compact Muon Solenoid Experiment

The **Compact Muon Solenoid** (CMS) experiment is a general purpose experiment located at the **LHC** point 5, near the village of Cessy, France. It was designed to be a high performance detector studying collisions at its centre. It is composed of several subsystems in a classic onion shaped structure. A diagram of the experiment can be found in figure 1.6.

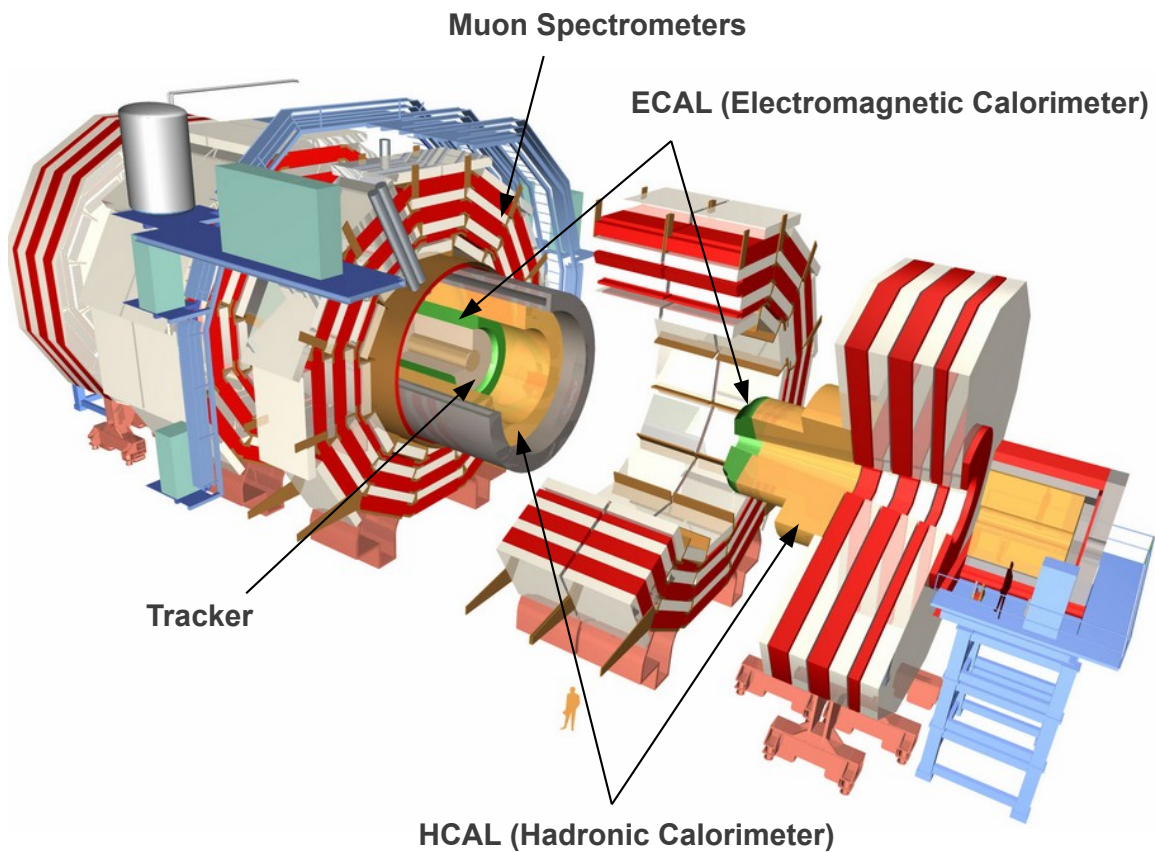


Figure 1.6: Diagram of CMS experiment showing the experiment in an open configuration and highlighting the position of its sub-detectors [14].

The main driving motivation for its design was to investigate the electroweak symmetry breaking and the Higgs mechanism at the design time was presumed to be the most likely explanation. Many alternative theories to the standard model predict new particles which could be observed at the TeV scale, CMS as a multi-purpose experiment is well suited to search for these new scenarios. If found, such new physics may allow us to understand some of the currently open questions in particle physics, like providing a particle candidates for dark dark matter. Further more, some of these possible new

physics signals could point the way towards a grand unified theory. CMS is also capable of operating while the LHC is colliding heavy ions and has a rich program covering the study of matter at extreme temperatures, densities and parton momentum fraction (low-x).

The requirements imposed on the CMS design to meet its physics goals can be summarized in the following table [6, 15]:

- Good muon identification and momentum resolution over a wide range of momenta and angles, good dimuon mass resolution ($\approx 1\%$ at 100 GeV), and the ability to determine unambiguously the charge of muons with $p_T < 1$ TeV.
- Good charged-particle momentum resolution and reconstruction efficiency in the inner tracker. Efficient triggering and offline tagging of τ 's and b-jets, requiring pixel detectors close to the interaction region.
- Good electromagnetic energy resolution, good diphoton and dielectron mass resolution ($\approx 1\%$ at 100 GeV), wide geometric coverage, π^0 rejection, and efficient photon and lepton isolation at high luminosities.
- Good missing-transverse-energy and dijet-mass resolution, requiring hadron calorimeters with a large hermetic geometric coverage and with fine lateral segmentation.

The final detector design fulfils all these requirements. The experiment is compact compared to the other LHC experiments being 22 m long and 15 m in diameter. Although small, it is the heaviest of the four big detectors at 12500 tonnes. Its high density is a direct consequence of it producing the highest magnetic field at 4 T and therefore needing more material for it to be contained in its return yoke.

1.2.1 Geometry and conventions

The adopted coordinate system has its origin in the center of CMS where the nominal collision point is located, the y -axis points vertically upwards, and the x -axis points radially inward in the direction of the centre of the LHC. The z -axis points along the beam line towards the Jura mountains from the LHC point 5. The azimuthal angle ϕ is measured from the x -axis in the x - y plane. The polar angle θ is measured from the z -axis.

We define pseudorapidity as $\eta = -\ln(\tan(\theta/2))$. All transverse quantities, like the transverse momentum (p_\perp), are measured in the transverse plane of beam axis. The imbalance of energy is also measured in the x - y plane and is denoted as E_\perp^{miss} .

1.2.2 Inner tracking system

The inner tracking system is the closest detector to the beam axis and the interaction region [16, 17]. Its function is to measure the trajectory of all charged particles with momentum above 1 GeV being produced at each LHC collision. With the help of the strong magnetic field produced by the CMS magnet, particle trajectories are bent allowing for charge and momentum determination. With the resulting tracks is it then possible to determine the primary vertex as well as secondary vertexes like other lower energy proton-proton collision or displaced vertexes from the decay of long lived particles like B mesons.

Building a tracking system for an experiment at the LHC is very challenging. Such system at design luminosity will be hit by an average of 1000 particles at a rate approaching 40 MHz. It needs to be a fast, efficient, high granularity detector, radiation hard and as thin as possible to not deflect the incoming particles trajectory. At each layer the occupancy should be of the order of 1% or lower. This design requirements have lead to a tracker design entirely based on silicon detector technology.

The volume near the interaction point can be split according to the charged particle flux into three regions:

- $r < 10$ cm: highest particle flux, up to $\approx 10^8 \text{ cm}^{-2}\text{s}^{-1}$ at $r \approx 4$ cm, pixel detectors are used. The pixel size is $\approx 100 \times 150 \mu\text{m}^2$, which translates into an occupancy of 10^{-4} per LHC bunch crossing.
- $20 < r < 55$ cm: particle flux decreases enough to use silicon micro-strips with a minimum cell size of $10 \text{ cm} \times 80 \mu\text{m}$, leading to an occupancy of $\approx 2 - 3\%$ per LHC bunch crossing.
- $50 < r < 110$ cm: most outer region of the tracker, particle flux is low enough to use larger pitch silicon micro-strips. The maximum cell size is of $25 \text{ cm} \times 180 \mu\text{m}$, and occupancy is of the order of $\approx 1\%$.

The CMS tracker final configuration is composed of a pixel detector with three barrel layers at radii between 4.4 cm and 10.2 cm and 2 disks on each side of the barrel. And a

silicon strip tracker with 10 barrel detection layers extending up to 1.1 m with 3 plus 9 disks on each side of the barrel. A schematic of this detector module distribution can be found at figure 1.7. This detector has an acceptance covering up to pseudorapidity of $|\eta| < 2.5$ and has a total active area of about 200 m^2 making the largest silicon tracker ever built.

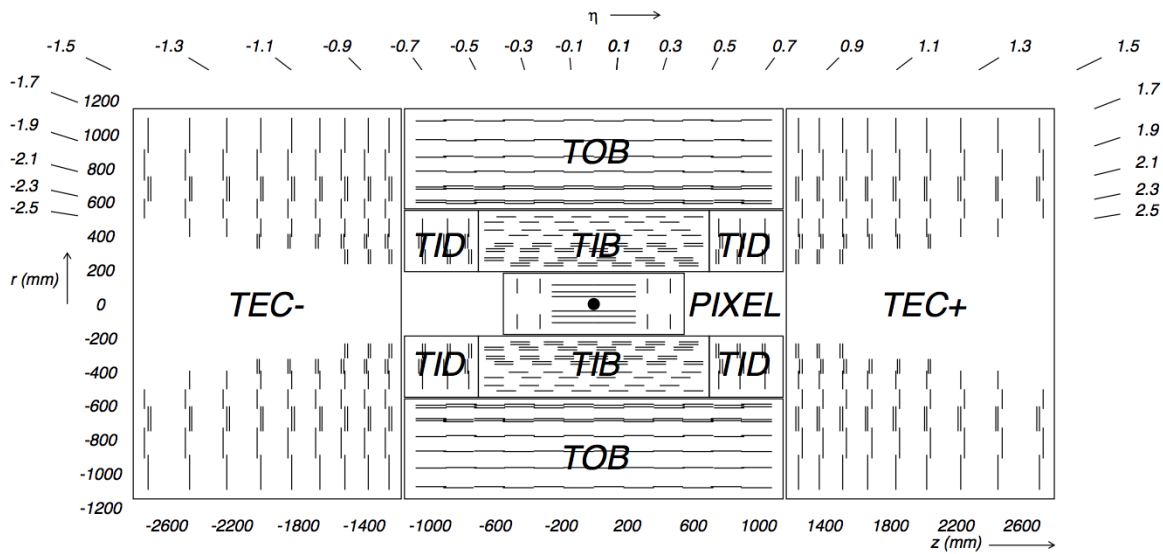


Figure 1.7: Schematic cross section of the CMS tracker [6]. Each line represent a detector module. Double lines represent dual surface back-to-back detector modules. The inner tracker components are shown components: **Tracker Endcaps (TEC)**, **Tracker Outer Barrel (TOB)**, **Tracker Inner Disks (TID)**, **Tracker Inner Barrel (TIB)** and **Pixels**.

1.2.3 Electromagnetic Calorimeter

The **Electromagnetic Calorimeter (ECAL)** is the detector responsible for measuring the energy of electrons and photons [18, 19]. It is an hermetic energy measurement system comprised of 61200 lead tungstate ($PbWO_4$) crystals mounted in the barrel and 7324 crystals in each of the 2 endcaps and it has an acceptance up to $|\eta| < 3.0$.

Lead tungstate has a fairly high density (8.28 g/cm^3), has a short radiation length (0.89 cm) and a small Moliere redius (2.2 cm). The crystals also have a fast scintillation decay time emitting 80% of the light yield in 25 ns (the minimal bunch crossing time at the LHC). This characteristics make it a good choice for an electromagnetic calorimeter allowing a compact design with fine granularity. However, this crystals emit a fairly low light yield ($30 \gamma/\text{MeV}$) which requires the use of photo-detectors with intrinsic gain

which will perform well inside a magnetic field. In the barrel region silicon **Avalanche photo-diodes (APD)** are used and **Vacuum Photo-Triodes (VPT)** are used in the endcaps. To guarantee good response from both crystals and **APD** it is necessary to have system thermal stability, with the goal being temperature variation of less than 0.1°C .

The barrel section, the **ECAL Barrel (EB)**, has an inner radius of 129 cm and is composed of 36 identical “supermodules”, each covers the barrel length and corresponding to a pseudo-rapidity interval of $0 < |\eta| < 1.479$. The crystals are quasi-projective (the axes are tilted at 3° with respect to the line from the nominal vertex position) and cover 0.0174 (i.e. 1°) in $\Delta\phi$ and $\Delta\eta$. The crystals have a front face cross-section of $\approx 22 \times 22 \text{ mm}^2$ and a length of 230 mm, corresponding to $25.8 X_0$.

The endcap section, the **ECAL Endcap (EE)**, is at a distance of 314 cm from the vertex and covering a pseudorapidity range of $1.479 < |\eta| < 3.0$, are each structured as 2 “Dees”, consisting of semi-circular aluminium plates from which are cantilevered structural units of 5×5 crystals, known as “supercrystals”. A diagram of the **ECAL** can be found on figure 1.8.

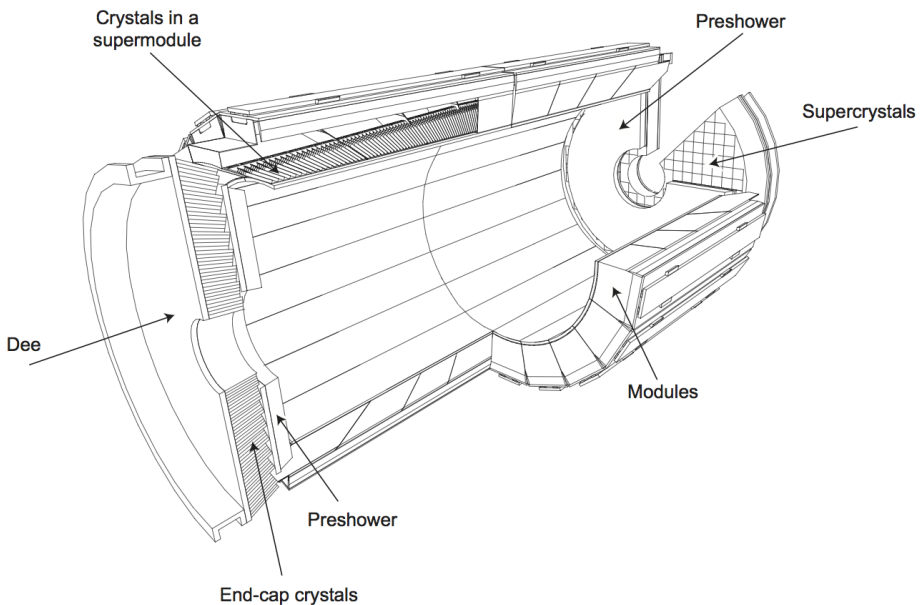


Figure 1.8: Diagram of the ECAL layout illustrating the positions of its components [6].

The energy resolution of the **ECAL** can be expressed as:

$$\frac{\sigma}{E} = \frac{S}{\sqrt{E}} \oplus \frac{N}{E} \oplus C \quad (1.2)$$

Here E is the energy of the incoming particle, S is the stochastic term which quantifies the fluctuations in scintillation and lateral containment of the shower, N the noise term which relates with electronics and digitisation process and finally C is a constant term that quantifies the non-uniform longitudinal response and inter-calibration errors. These parameters have been measured to be $S = 0.028 \text{ GeV}^{1/2}$, $N = 0.12 \text{ GeV}$ and $C = 0.003$ with the help of an electron beam [20] and in the absence of magnetic field.

Preshower detector

The CMS Preshower is a detector located in each endcap covering the fiducial region of $1.653 < |\eta| < 2.6$. Its mission is to identify neutral pions decay, help to identify electrons against minimum ionizing particles and improve electron and photon position determination.

This detector is sampling calorimeter composed by two layers of lead radiators each followed by silicon strip sensors. The lead layers have the function of forcing the incoming particles to initiate an electromagnetic shower. The first lead layer had $2X_0$ while the second had $1X_0$, which results in 95% of the single incident photons starting their shower before hitting the first sensor [6]. The shape of the lead layers edge matches the ECAL crystal behind them to facilitate calculations at the Level 1 Trigger (L1T).

Each silicon sensors have an active area of $61 \times 61 \text{ mm}$ and are $320 \mu\text{m}$ thick. The sensors are divided into 32 strips each with 1.9 mm . The preshower system has a total thickness of 20 cm and had 137000 individual read-out channels.

1.2.4 Hadronic Calorimeter

The Hadronic Calorimeter (HCAL) is a sampling calorimeter which is designed to measure the properties of hadron jets and indirectly neutrinos or other undiscovered particles that would result in apparent missing energy [21]. The design of the Hadronic Calorimeter (HCAL) was strongly influenced by the choice of the magnet parameters since most of the calorimetry is inside of the magnet. A diagram of the HCAL subsystems and their location inside CMS can be found in figure 1.9.

The HCAL Barrel (HB) covers the region up to $|\eta| < 1.3$ and is limited from the beam side by the ECAL at radius $r = 1.77 \text{ m}$ and outwards by the magnet at radius $r = 2.95 \text{ m}$. This is a strict limitation on the amount of absorber material to be used. This detector is

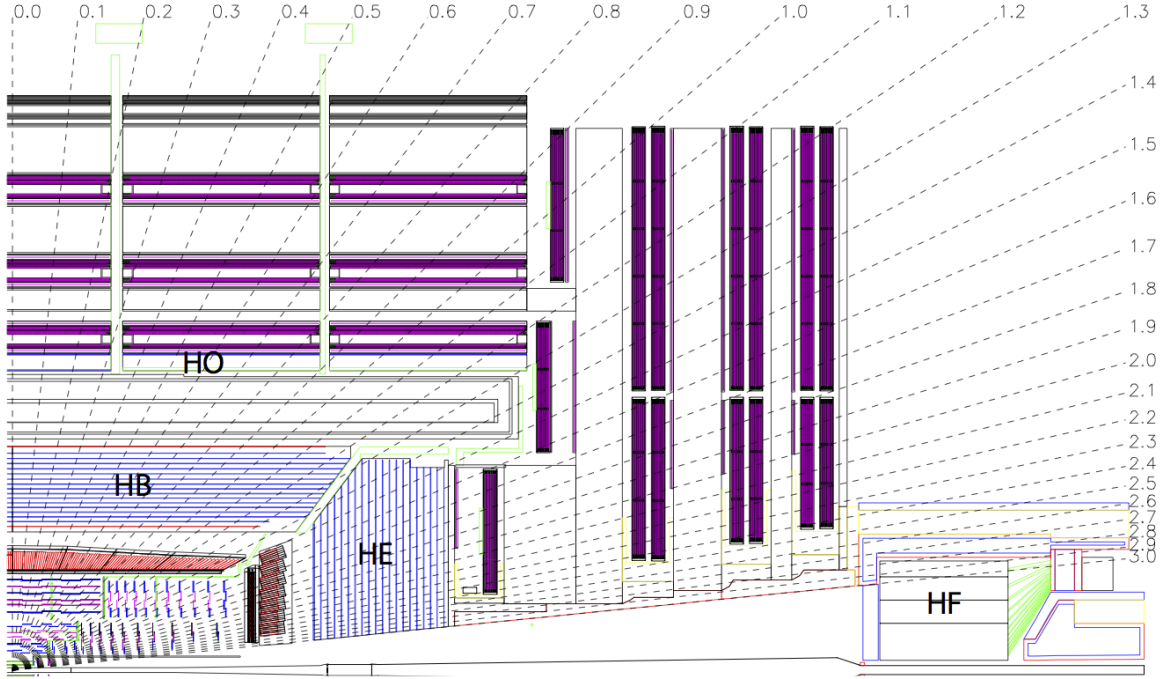


Figure 1.9: Longitudinal view of the CMS detector highlighting the location of the **HCAL** components: **HCAL Barrel (HB)**, **HCAL Endcap (HE)** **HCAL Outer (HO)** and **HCAL Forward (HF)** [6].

composed of 36 identical azimuthal wedges split in two half-barrels. They are constructed of brass absorber plates alternated with plastic scintillator. Brass has a short interaction length ($X_0 = 16.42$ cm) and is non-magnetic. The detector is composed of 2304 towers with a segmentation of $\Delta\eta \times \Delta\phi = 0.087 \times 0.087$ which corresponds to the same area of a 5×5 arrays of **ECAL** crystals.

To improve the measurement capability, an outer calorimeter, the **HCAL Outer (HO)**, is placed outside of the magnet as a *tail catcher*. It increases the effective thickness of the hadronic calorimeter by over 10 interaction lengths. This detector covers the range $|\eta| < 1.26$, it is composed of iron absorber and scintillator and is subdivided into sectors that cover 30° azimuthal angle in each of the barrel wheels.

The **HCAL Endcap (HE)** covers the range of $1.3 < |\eta| < 3.0$. It is composed by 2034 towers with a 14 towers segmentation in η and 5° segmentation in ϕ . The 8 inner most towers the segmentation is 10° in ϕ , whilst the η segmentation increases in η from 0.09 to 0.35.

Additionally, to extend acceptance to $|\eta| < 5.2$ the **HF** is installed at 11.2 m from the interaction point providing excellent hermeticity for E_{\perp}^{miss} measurement. Its steel

absorber is 1.65 m deep and has quartz fibres running through it, parallel to the beam line. The energy measurement is made via Cerenkov light produced by the incoming particles inside the fibres. There are 13 tower in η with segmentation of $\approx \Delta\eta = 0.175$ except the lowest η tower with $\approx \Delta\eta = 0.1$ and highest η tower with $\approx \Delta\eta = 0.3$. The segmentation in ϕ is of $\Delta\phi = 10^\circ$ except in the highest η towers which is $\Delta\phi = 20^\circ$. There are a total of tower 900 per HF module.

Similarly to the ECAL the energy resolution HCAL was tested using a test beam of single charged pions [20], and it was obtained that:

$$\frac{\sigma}{E} = \frac{94.3\%}{\sqrt{E}} \oplus 8.4\%. \quad (1.3)$$

1.2.5 Solenoid Magnet

The design requirements for correct charge assignment and p_T determination for charge particles and specially muons drive the magnet parameters choice. For muons, unambiguously charge determination requires momentum resolution of $\Delta p/p \approx 10\%$ at $p = 1\text{TeV}$. This requirements are specially difficult to obtain in the forward regions but with the correct length/radius ratio can be obtained with a modestly sized solenoid magnet but with large field [10, 22].

The choice of the CMS collaboration was to build a Niobium-Titanium (NbTi) superconducting solenoid magnet which has been design to operate at fields up to 4 T it has a diameter of 6 m and a length of 12.5 m at maximum field the stored energy reaches 2.7 GJ. Typically, the magnet is only run at 3.8 T in order to maximize its lifetime. To contain such an enormous magnetic flux a 10 kt return yoke envelopes the magnet with 5 wheels in the barrel region and 2 endcaps composed of 3 disks closing the sides [6]. A summary of the most important magnet parameters can be found at table 1.2.

1.2.6 Muon System

The muon detection is an important part of the mission of CMS [23]. Muons are fairly easy to detect when compared with other elementary particles and are only rarely produced in proton-proton collisions. To take the example of the SM Higgs boson, while the decay mode involving a pair of Z bosons is fairly unlikely compared with other decays

Parameter	Value
Field	4 T
Inner Bore	5.9 m
Length	12.9 m
Number of turns	2168
Current	19.5 kA
Stored Energy	2.7 GJ
Hoop Stress	64 atm

Table 1.2: Parameters of the CMS superconducting solenoid [10]

the Z bosons can decay into 4 muons. This decay while rare does not have significant backgrounds making it a "golden channel" for discovery, which indeed was proven the case [24]. Many other models, like SUSY, use muon final states in their searches exactly for the same reason. The CMS muon system is composed of 3 types of gaseous detectors depending on they location and momentum reconstruction needs. A diagram of the disposition of this system inside CMS can be found on figure 1.10.

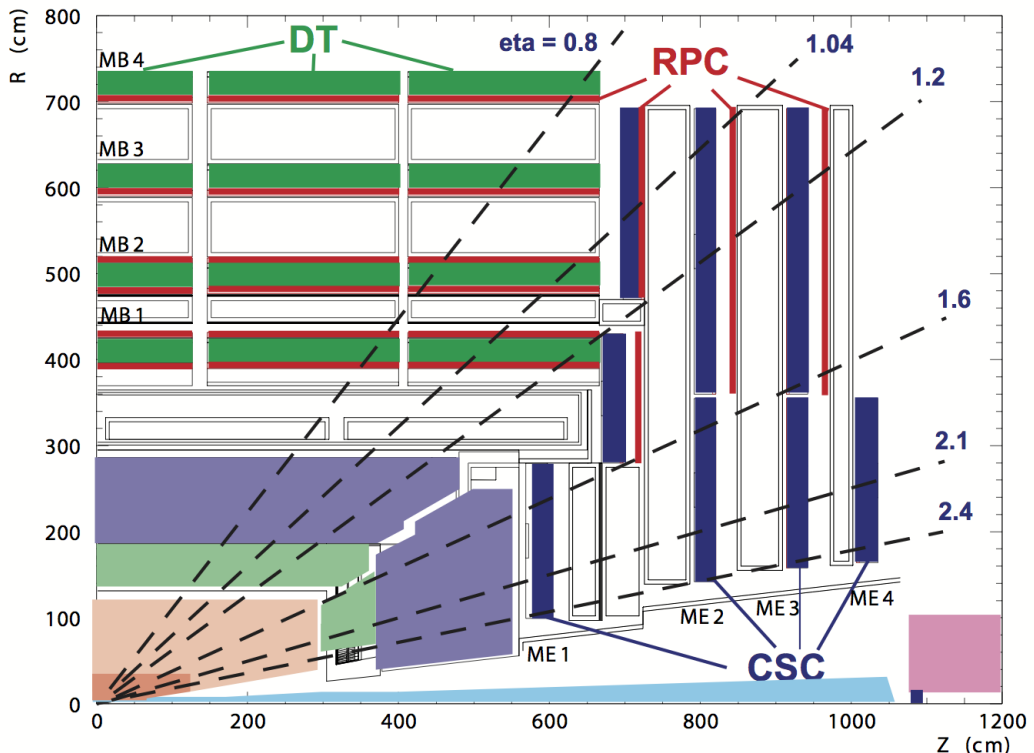


Figure 1.10: Diagram of the CMS muon systems. The location of each muon chamber for each subsystem is showed [10].

In the barrel and up to $|\eta| < 1.2$, Drift Tube (DT) are used. since the neutron background is small and the field is constant. This system is composed 250 chambers and is arranged in 4 concentric cylindrical layers which are installed inside of the return yoke. This chambers have a total of 172000 wires with a length of 2.4 m which are housed inside of tubes filled with a mixture of argon and carbon-dioxide. Each of the wheels of the barrel is split into 12 sectors covering 30° azimuthal angle. The maximum gas ionization drift is of 2.0 cm and results in a single point resolution is $\approx 200 \mu\text{m}$ per wire. For each station each measured muon the ϕ resolution is better than $200 \mu\text{m}$ and direction resolution is $\approx 1 \text{ mrad}$.

In the endcaps Cathode Strip Chamber (CSC) are used in the region between $2.4 > |\eta| > 0.9$. Here, muon and background rates are high and the magnetic field is not uniform. This system has fast response and is radiation resistant. It is composed by 468 chambers arranged in 4 stations per side. Each chamber is trapezoidal in shape and made of 6 gas gaps and covers either 10° or 20° in ϕ . Each gap contains a plane of cathode strips and a plane of anode wires. For each chamber the spacial resolution is of the order of $200 \mu\text{m}$ and the angular resolution is $\approx 10 \text{ mrad}$ in ϕ .

Finally the Resistive Plate Chamber (RPC) covers the $|\eta| < 1.6$ range. This system overlaps with the 2 other muon systems. It is very fast with an ionization event being much faster than the bunch crossing time. This fast response allows, in conjunction with a dedicated trigger system, to select the correct bunch crossing associated with the detection of a muon. In the barrel there 480 rectangular chambers arranged in 4 stations with 6 RPC layers (2 layers are present in the 2 stations closest to the beam pipe). In the endcaps there are 3 RPC disk shaped stations on each side, which are composed by trapezoidal shaped detectors.

The combined muon system offline momentum resolution is of the order of 9% for small values of η and p and for transverse momenta of up to 200 GeV. At higher energies of around 1 TeV the standalone momentum resolution is in the range of 15-40% depending on $|\eta|$. These values are limited by the muon multiple-scattering before arriving to the muon system. If we combine the tracker information into a global fit the resolution for lower p_T tracks improves an order of magnitude while at higher momenta (around 1 TeV) it is of about 5%, which is well inside the CMS design requirements.

1.2.7 Data Acquisition System

The CMS Data Acquisition (DAQ) system is designed to process, analyse and ultimately store the information collected by the detector [25]. The LHC produces bunch crossings at a rate of 40 MHz but we are only capable of storing between $10^2 - 10^3$ events per second. At design luminosity each collision will have an average of over 20 simultaneous collisions and produce a zero-suppressed data payload of around 1 MByte. To reduce the event rate to completely retrieve from the detector buffers a first level of trigger was developed. This hardware system reduces the amount of events to be processed to a maximum of 100 kHz. Even with this event suppression the DAQ has to retrieve and move $\approx 100 \text{ GBytes}^{-1}$ from the detector to the surface. This data comes from approximately 650 data sources and has to be merged into a single event package. The information is then passed to a computer farm where a software filters serve as a second level of trigger. In this system the event rate is further reduced up top a factor of 1000 making the output rate compatible with what can be saved into permanent storage. A diagram of this system can be found on figure 1.11.

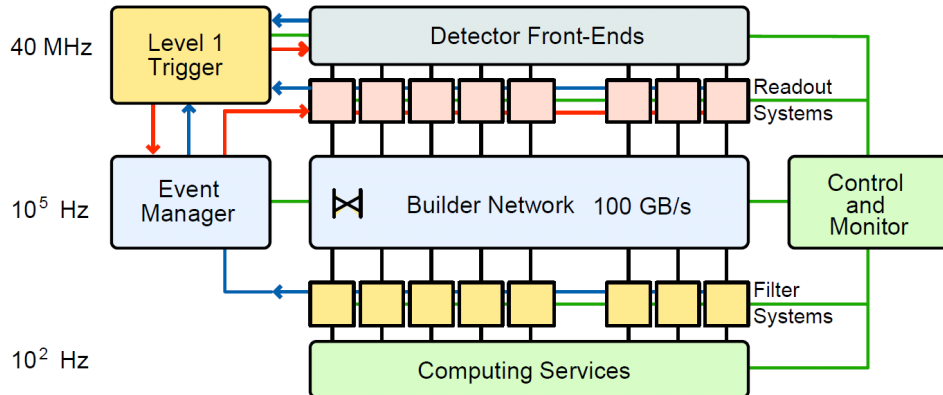


Figure 1.11: Diagram of the CMS DAQ system. Data flow is showed as the lines connecting each electronics or computing units [6].

1.2.8 Trigger System

As described on the previous section the CMS trigger system is responsible for selecting which collisions are recorded in real-time. We can only save $10^2 - 10^3$ events per second with the current systems. This implies that the trigger system needs to obtain a data reduction of a factor of $\mathcal{O}(10^6 - 10^7)$. This is achieved with a two level trigger system, the first is a dedicated hardware system named **Level 1 Trigger (L1T)** [26] and the second is

a commercial computer system running dedicated software called the **High Level Trigger (HLT)** [25].

Initially, all data is stored for 128 bunch crossing which corresponds to $3.2\ \mu\text{s}$. This is the time we have to make a first decision to keep or discard an event. This is the task of the **L1T** which has the target to reduce the data to a maximum rate of 100 kHz. There isn't enough time to get all the information from the detector, so only a coarse version of the calorimetry and muon systems data, and some correlation between them is accessed. With this information the **L1T** produces a set of particle candidates and energy sums over which custom user defined algorithms can use to filter events. A diagram of the **L1T** trigger components and the data flow across the system is present on figure 1.12.

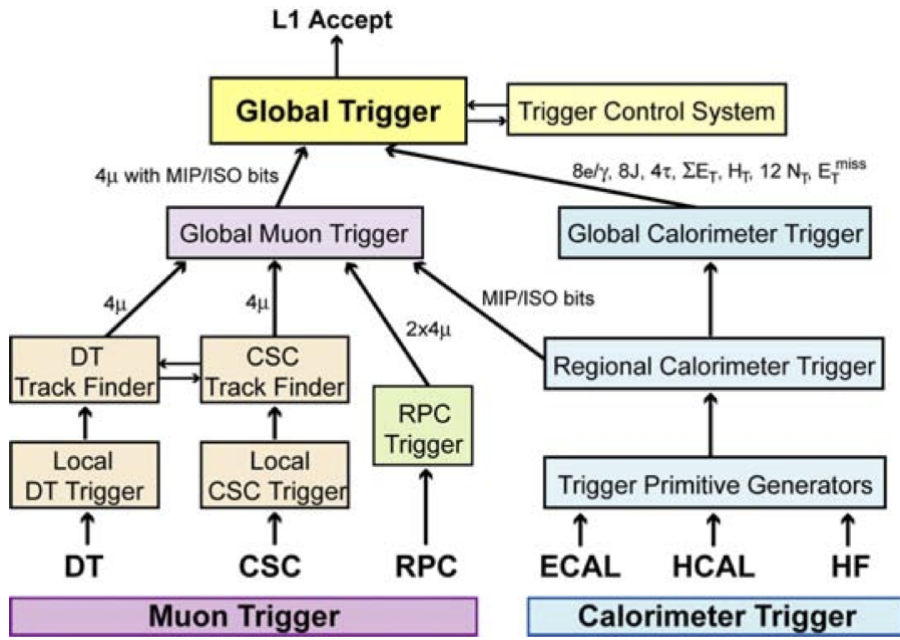


Figure 1.12: Diagram of the **L1T** system. The arrows indicate data flow and the number of particle candidates at each step is indicated [6].

The **High Level Trigger (HLT)** receives events accepted by the **L1T** and needs to perform further event reduction of $\mathcal{O}(10^3 - 10^2)$ to a final output rate of $\mathcal{O}(10^{2-3})\ \text{Hz}$. This system is composed of standard computing hardware in the form of computing farm with $\approx 15\text{k}$ **Central Processing Unit (CPU)**. This system, using the additional latency created by the **L1T** event selection, is able to make use of the complete detector information including the tracker data. More sophisticated and precise algorithms are therefore possible which can be tailored to select any desired physical final state.

Event selection algorithms at both the L1T and HLT are frequently updated during data taking. The selection thresholds may be tuned in order to control the rate with the changes of LHC luminosity. Novel methods or strategies to identify particles more efficiently can be implemented, like PU subtraction or new calibrations. Analysis groups may also show interest in recording new event final final states for which new selection criteria may be developed. The set of algorithms used for data taking is normally referred as the *trigger menu*.

After events pass both levels of the trigger they are recorded into permanent storage. During 2012-13 operation, two output streams were saved. The *prompt data stream*, with a rate of approximately 300 Hz, was composed of high priority trigger paths which were immediately reconstructed. And the *parked data stream*, with an average rate of 600 Hz, was stored without reconstruction. This data waited until computing resources were free to go through reconstruction [27]. This process was finalised a few months after the LHC Run I was finished.

Even with such measures to reduce the data to be stored, each LHC experiment records several petabytes of data every year in addition to similarly sized amounts of simulated events.

1.2.9 Computing

The quantity of data produced by the LHC and the necessary processing capability is so big that it would be difficult to have all computing resources in a single place. For this reason a tiered system was developed, where all participating computing sites are connected and have specific roles and responsibilities in the data taking, processing and storing. This global computing system is know as the Grid [28].

The CERN Data Centre is the Tier 0 of this network, all data produced by the LHC experiments is handled by this facility. Only about 20% of the total capacity of the Grid is hosted here, but CERN Tier 0 has the very important mission of safe keeping all the raw data produced by the experiments. It also has the task of doing the first attempt of event reconstruction, which is the process identifying meaningful physics objects in data.

There are 7 CMS Tier 1 computer centres around the world. They are responsible to store a proportional amount of raw and reconstructed data. If any reprocessing of the data is needed, this centres are responsible for this task and storing the resulting output as well. Tier 1 centres also host simulated data and distribute it to Tier 2 centres.

Local research centres like universities or scientific laboratories are normally at the Tier 2 level. These centres have the responsibility of handling a proportional share of simulated data production and reconstruction. Currently there are over 150 Tier 2 centres around the world.

Individual computers or local clusters without any formal engagement with the Grid structure, are considered to be the Tier 3 level of the Grid.

1.2.10 Level 1 Trigger: Stage I Upgrade

An extensive upgrade program for the L1T electronics was planned and is being executed in order to cope with the increase of luminosity and pile-up predicted for the period after [Long Shutdown 1 \(LS1\)](#) [29, 30]. The center-of-mass energy has almost doubled from 8 TeV to 13 TeV, instantaneous luminosity will also increase as will average pile-up. Also, the bunch separation has changed from 50 ns to 25 ns making out-of-time pile-up a significant problem.

To ensure physics performance during 2015 and beyond only a partial upgrade was executed for the 2015 run which is known as the *Stage-1* upgrade. The main feature of this upgrade program is the replacement of the existing [Global Calorimeter Trigger \(GCT\)](#). Two key enhancements were possible:

- Event-by-event pile-up energy subtraction for jets reconstruction, e/γ isolation, τ isolation.
- Smaller feature size τ candidates, which will have significantly better energy estimation and background rejection.

The intermediate system will have significantly better performance than the now legacy system. The full 2016 calorimeter trigger system will additionally provide finer granularity which will lead to increased position and energy resolution.

Chapter 2

Technical work

The author as member of the Compact Muon Solenoid (CMS) collaboration was required, like all other members, to perform service work in order to become member of the CMS author list. This requirement has been fulfilled with work for the Level 1 Trigger (L1T) system. Field work component was performed by doing shifts as Trigger and Shift Leader in the experiment control room and on call shifts as the Trigger Detector On Call (DOC) expert. Another important contribution was the work as a software developer for the L1T Data Quality Monitoring (DQM) system. The authors contributions lead his appointment for two years to the position of coordinator of the CMS L1T DQM software development team. This chapter describes the tools developed and used for online monitoring of the L1T during 2012-13 data taking. These tools were partially ported to the offline monitoring and were the basis for data certification for physics analyses.

2.1 Data Quality Monitoring

The Data Quality Monitoring (DQM) is a critical monitoring system that has an important role in detector and operations efficiency. It is also important in the certification of recorded data for physics analysis [26, 31]. The DQM system is an end-to-end solution that provides tools to create, fill, display and archive histograms and scalar monitors. It provided the ability to monitor the detector and Data Acquisition (DAQ) in real-time, analyse the reconstruction process, validate the experiment's software releases and its simulated data. The purpose of this system is to identify problems or errors in both hardware and software as early and accurately as possible.

2.1.1 Online Monitoring

The online **DQM** system is composed of several applications that are part of the **CMS** data processing work flow. The software is executed at the **CMS** point 5 computing cluster. Applications fall into two categories: *high level trigger modules* and *data quality monitoring modules*. The *high level trigger modules* are run directly in the **High Level Trigger (HLT)** filter farm and can only produce a limited number of histograms with the purpose of monitoring that system or specific **HLT** path. The *data quality monitoring modules* run over event coming from a dedicated **DQM** event stream with a rate of 5 – 10 Hz. These events contain only the raw detector and trigger information. Each subsystem has its own application which can analyse all events from the stream or filter a subset with a predefined trigger selection. At the end of every luminosity section, which corresponds to 23.31 s, histograms are gathered from the nodes where the applications are run and are merged together. The results are showed in real time in a web based application which is accessible by the shift crew and on call experts.

2.1.2 Offline Monitoring

The offline **DQM** is used in numerous workflows including monitoring of the event reconstruction process, alignment and calibration validation, **CMS** software release validation, etc. For all this task a standardized two step process is run.

In the first step histograms are produced in the same computing jobs of the task to be monitored and stored along with the rest of the event data. This happens in multiple simultaneous jobs which depending on the task can be at Tier 0 or Tier 1 level.

In the second *harvesting step*, the histograms are extracted from the event data and summed together. The resulting histograms contain the full event yields from each run for each processed dataset. Applications running at this step have access to the detector conditions from the **Detector Control System (DCS)** and the **DAQ** and can produce new histograms such as summaries of the relevant quantities for each run.

2.2 Level 1 Trigger Data Quality Monitoring

The **Level 1 Trigger (L1T) Data Quality Monitoring (DQM)** is composed of four applications. The first two application run as part of the online **DQM** system with the

mission of monitoring the trigger and trigger emulation in real-time. The second pair of applications runs in the offline **DQM** system as part of the (re-)reconstruction workflow with the main function of providing information for physics data certification.

The first of the two online applications directly monitors the operation of the trigger. Each trigger subsystem produces plots of its own relevant quantities including information on the produced objects which allows to pin-point the origin of problems. Additionally, a set of monitoring tools observe the final objects and global behaviour of the system. Key aspects are analysed such as the value of reference algorithm rates, synchronization of firing, finding regions of the detector that show unexpected high/low rate. The second online application compares the results of the trigger against a real-time software emulation of the system which should allow quick detection of trigger miss configuration or degradation of quality of operation.

Both offline monitoring applications replicate the analysis preformed by their online counterparts but over a the complete recorded dataset for each run.

In the next sections we will focus on the trigger monitoring tools that the author developed or improved.

2.2.1 Rates Monitoring

The rates monitoring tool has the objective of inspecting the firing rate of each **L1T** object category. At the beginning of each run the **L1T** menu is analysed and for each object category the lowest thresholds unprescaled algorithm is selected. If no unprescaled algorithm is available the lowest prescale and threshold trigger is selected. If the selected trigger algorithms are η restricted a warning is showed in the produced histograms to identify that the tests performed do not cover the full acceptance of the monitored object. The following categories of objects can be monitored: Electron-Gamma, Isolated Electron-Gamma, Central Jets ($|\eta| < 3$), Forward Jets ($3 < |\eta| < 5$), All Jets ($|\eta| < 5$), Taus, Muon, total energy (ETT), total energy in jets (HTT), missing energy (ETM) and jets missing energy (HTM).

When the algorithms to be monitored are determined the tool retrieves from an external database the expected algorithm cross section as a function of the instantaneous luminosity. These functions are updated daily by fitting runs from the previous days with similar condition. This task is executed by the **Web base Monitoring (WbM)** which is a **CMS**

monitoring system which runs in parallel to the **DQM**. The algorithm cross section for each luminosity section is calculated with following equation 2.1.

$$\sigma_{\text{Algo}} = \frac{\text{Prescale}_{\text{Algo}} * \text{Avg. Rate}_{\text{Algo}}}{\text{Avg. Instantaneous Luminosity} * (1 - \text{CMS Dead time fraction})} \quad (2.1)$$

The measured value is compared with prediction from previous runs for each luminosity section. The monitor presents this results in histograms with the measured value and the relative value to prediction. An example of this histograms can be found in figure 2.1

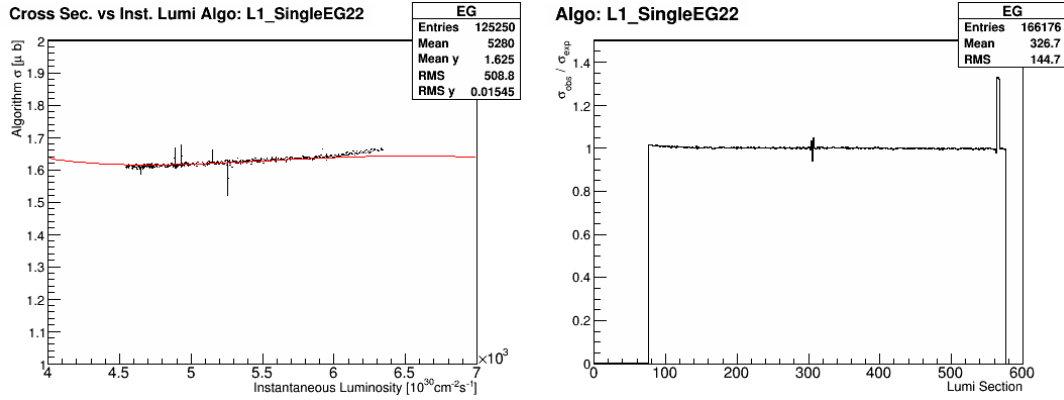


Figure 2.1: Monitoring plots produced by the **L1T** online rates monitoring tool for run 207269 and the Electron-Gamma object category. The automatically selected algorithm was **L1_SingleEG22** for this run. On the left histogram the algorithm cross section as a function of instantaneous luminosity is plotted. The red line is the prediction obtained from fitting data from previous runs while the black points are the measurements for this run. On the right histogram the fraction of the measured value over the prediction is showed as a function of the luminosity section.

Automatic tests are configured to monitor the produced histograms and flag as bad the luminosity sections that show deviation from prediction above 20%. Marking a specific luminosity section as bad does not invalidate its use for physics analysis, but references it for further investigation by the **CMS** shift crew or certification experts.

2.2.2 Synchronization Monitoring

The synchronization monitoring tool has the objective of assessing if each **L1T** object category is being produced and associated with the correct bunch crossing. Similarly to the **L1T** rates monitoring tool described in the previous section, in the beginning of each

run we select the lowest thresholds unprescaled algorithm for each object category. If none are available the algorithm with lowest prescale and lowest threshold is selected.

The information of which bunch crossings are filled is retrieved at the beginning of each run by CMS. That information is stored in a database at point 5 and later replicated to the CMS offline conditions database. At the same time, the synchronization monitoring tool determines the Large Hadron Collider (LHC) fill number from the L1T Global Trigger (GT) system. Data from the LHC is obtained via the Data Interchange Protocol (DIP) which allows exchange of information between detector and accelerator. With this information the bunch crossing information is retrieved from the Online Master Database System (OMDS) when running online and from Offline Reconstruction Condition DB ONline (ORCON) when running offline.

When selected events are desynchronized from the correct bunch crossing at the L1T level, these events will appear empty from the HLT and offline perspectives. Therefore it is unlikely that they will pass any HLT triggers, making it very difficult to spot this type of problems. For this reason the synchronization monitoring looks only at events that come from special HLT trigger, the HLT pass-through paths. These triggers are highly prescaled and only required that a specific L1T condition is fired. All available HLT pass-through paths of single object L1T trigger are monitored by this tool.

All events triggered passing HLT pass-through paths are analysed and all selected algorithms firing is compared to the actual LHC bunch crossing filling and the results are recorded. Additionally, for each event we query the GT about the LHC beam mode and if for any event the status is not Stable Beams, the luminosity section is immediately marked as bad.

Since we are running this monitoring only over the events that pass HLT pass-through paths a single luminosity section will typically not have enough statistics to take conclusions on the behaviour of the system. To provide reliable results at the end of each luminosity section it is decided if the current luminosity section has enough statistics by itself or needs to be grouped with the previous ones. Blocks of luminosity section are made until a minimum configurable number of events is reached for each individual monitored trigger. At this point the histogram of the fraction of events in time with bunch crossings is updated. If the LHC beam mode changes or the run ends, the current open luminosity sections block is closed with the current statistics. The histograms produced by this tool for run 207269 can be found in figure 2.2.

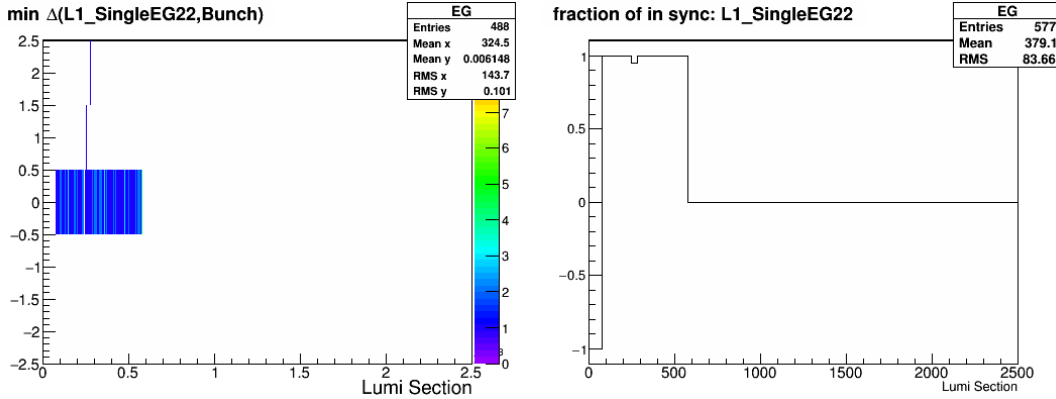


Figure 2.2: Monitoring plot produced by the L1TSync tool for L1 single electron/gamma object category, which is automatically monitoring algorithm L1_SingleEG22 for the run 207269. In the plots data points are the calculated trigger cross section as a function of instant luminosity and the line is the reference fit done from previous runs.

Similarly to the **L1T** rates monitoring tool, automatic tests are configured to flag as bad luminosity sections that show deviation from prediction above 20%.

2.2.3 BPTX Monitoring

The **Beam Pickup for Timing for the eXperiments (BPTX)** system is composed of two beam detectors located in each beam pipe 175 m upstream of the **CMS** experiment [6]. This detectors were designed to provide precise information about the bunch structure and timing of each beam and have sensitivity to time structures under 25 ns.

In early 2012 a problem was identified in the **L1T** where some events would fire on the bunch crossing before the actual event. It was discovered that this effect was most likely connect to sensors in the calorimeter system being directly hit by particles causing a large out-of-time signal. Unfortunately, the trigger has a set of rules intended to limit the event rate. They are necessary in order to allow for the necessary latency to extract the information from the detector in case a collision is accepted. One of these rules states that if a collision is accepted by the **L1T** the next 2 collisions are ignore by the system [26]. This means that if a specific event causes the **L1T** to fire on the previous bunch crossing, that event will be vetoed by trigger rules. To avoid losing interesting events due to this pre-firing problem the signal of both **Beam Pickup for Timing for the eXperiments (BPTX)** detectors logical AND was advanced by one bunch crossing and

connected to the trigger via a technical algorithm bit. This bit in turn was used to veto the **L1T** from firing.

Although this was a successful solution to this problem it caused preoccupation in the **Trigger Studies Group (TSG)** and **L1T Detector Performance Group (DPG)** groups. Since if the **BPTX** bunch detection threshold would be set too high this veto would be ineffective, leading to no bunches being detect and no veto being applied. If the **BPTX** bunch detection threshold would be set too low, residual amounts of protons or noise in the unfilled bunch spaces could lead to vetoing filled bunch spaces. The development and commissioning of a monitoring tool was requested as priority task.

A new tool was developed to compare the **LHC** filling scheme with the firing of the technical trigger associated with the **L1T** veto. Following the ideas of the **L1T** synchronization monitoring tool the same procedure was used to retrieve the **LHC** filling scheme and algorithm firing results. For each selected event the **GT** records the results of each **L1T** trigger algorithm for the two previous and two posterior bunch crossings. For this tool all five recorded bunch crossings in each event are compares with the **LHC** bunch structure. In this case we are interested in both efficiency, since low efficiency would mean that the **BPTX** bunch detection threshold would be too low. And miss fire rate, which would be associated with a **BPTX** bunch detection threshold would being too high. Examples of the histograms produced by this tool can be found in figure 2.3.

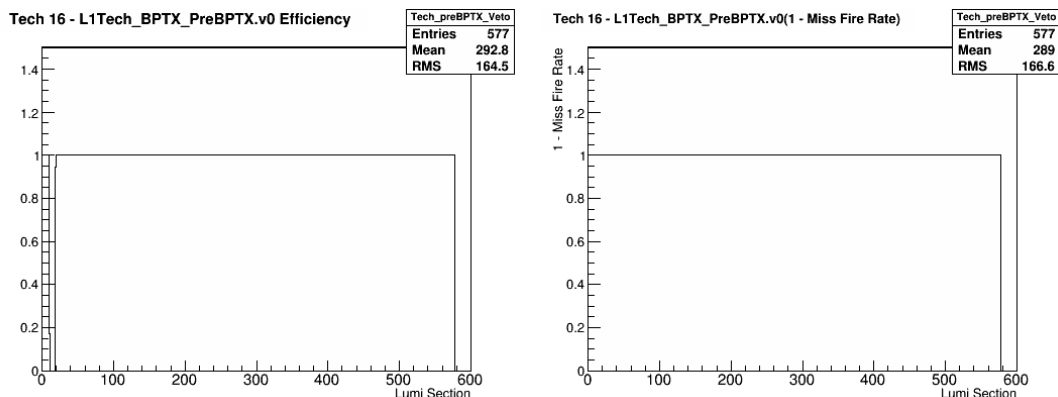


Figure 2.3: Monitoring plot produced by the **L1T BPTX** monitoring tool for CMS run 207269. On the left the **BPTX** veto efficiency in relation to the **LHC** fill bunch structure is showed. On the right for the same algorithm 1 – Miss Fire fraction is showed.

Implementation Tests

To test that the **BPTX** monitoring tool would be successful in detecting the possible failure of the **BPTX** system a field test was necessary. During run 207269 in which real data recorded the author with the permission of the **L1T DPG** disabled the technical **L1T** bit associated with the **BPTX AND** signal advanced by one luminosity section which was configured as a veto in the system. The bit was kept disable for a few luminosity sections which was promptly identified by the monitoring tool as it can be seen in figure 2.4.

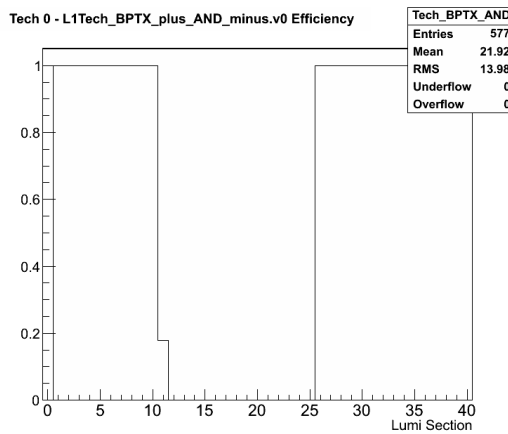


Figure 2.4: Detail of **L1T BPTX** monitoring tool histogram for veto efficiency during its field test at run 207269. The monitored bit was disabled manually leading to the monitored drop off efficiency.

After this successful test the trigger shifter instruction were updated to include this histogram in the periodic checks to be done.

2.2.4 Occupancy Monitoring

The occupancy monitoring tools objective is to identify regions of detector where the trigger system response has degraded. A region is considered *dead* if the number measurements is null or its rate is consistently smaller than what would be expected for that area. Alternatively, a region can become *hot* if the measurements rate is consistently bigger than expected for that area. This tool aims at identifying both of these categories of problems by analysis histograms produced by the trigger subsystems.

The main idea behind these tool is to use the η and ϕ symmetries of the physics processes and experimental design. The collisions in **CMS** happen in the centre of the experiment with beams of the same energy colliding head-on. Additionally, the detector is symmetric

to the beam lines transverse plane passing on the collision point and also to the beam line itself. Both these factors imply that the response in a strip of cells across ϕ at constant η should be the same on average in every cell and that response should be equivalent in a similar strip and constant $-\eta$.

The test consists of initially selecting an histogram of a quantity that is expressed in absolute event counts per region and that exhibits the described η and ϕ symmetries. The histogram is integrated for as many luminosity sections as necessary to have enough statistics for conclusive results. When enough statistics are gathered and starting from the centre, a strip of cells is defined along ϕ to one side of that symmetry line. The value of the median of the selected cells is determined. Each cell of the opposing strip is compared to this median with statistical tests tuned to detect significant deviations. If any tests are failed, the cell is marked as bad for the period of the histogram integration. We repeat the same procedure reversing the role of both strips. After all cells in the first strip pair is tested we move to the next two strips of cells in increasing η and repeat the procedure until all cells in the histogram have been tested. For histograms where the symmetry line fall in the middle of a strip of cell, that strip is tested against itself. The median is used to avoid bias from outliers like the *hot* or *dead* cells we are aiming to identify.

Cells which are already known to be problematic can be masked from this tool to avoid being always marked as bad and contributing to the calculation of the fraction of problematic cells.

Statistical hypotheses test

Since we are analysing histograms of absolute number of entries, like the location on L1T Electron-Gamma candidates, each cell will follow Poisson statistics [32]. The probability of obtaining an histogram cell with value x when the expected value is μ is expressed in equation 2.2.

$$P(x; \mu) = \frac{\exp(-\mu) \cdot \mu^x}{x!} \quad (2.2)$$

The implemented statistical tests will evaluate each cell over two hypotheses. The null hypothesis H_0 , considers that the cell is behaving as expected and that the average number of events is μ_0 . The alternative hypothesis H_1 , proposes that this is a problematic

cell with an average number of events of μ_1 . We can now define a test statistic T as the log-likelihood ratio of the two hypothesis as defined in equation 2.3.

$$T = \ln \frac{P(x, \mu_1)}{P(x, \mu_0)} \quad (2.3)$$

The test statistic $D = 2 \cdot T$ will be χ^2 -distributed on the limit of infinite sample size. Two tests need to be preformed for the *dead* and *hot* hypotheses. The relationship between μ_0 and μ_1 for both tests can be defined as $\mu_1 = f \cdot \mu_0$ where f is the factional deviation from μ_0 to flag a cell as bad. The following values were chosen, for *dead* cells $\mu_{\text{dead}} = f_{\text{dead}} \cdot \mu_0$ with $f_{\text{dead}} = 0.1$ and $\mu_{\text{dead}} = f_{\text{dead}} \cdot \mu_0$ with $f_{\text{hot}} = 2.0$ for *hot* cells.

A test efficiency of 99% with a fake rate of 1% were chosen as key parameters to constrain the the test behaviour, where efficiency is the probability of correctly identifying a problematic cell and fake rate is the probability of marking one or more cells as bad in a single histogram. The choice of these parameters defines the test threshold T_{crit} and implies a requirement on the minimum average number of events per cell depending on the number of bins per histogram.

If the test statistic T is above the critical value T_{crit} we reject H_0 and consider the cell as bad, if is it below T_{crit} we do not reject H_0 and consider the cell as good. The critical value is set by a choice of confidence level of finding a problematic cell and depends on μ_0 . To determine $T_{\text{crit}}(\text{DeadCell})$ and $T_{\text{crit}}(\text{HotCell})$ as a function of μ_0 two sets **Monte Carlo (MC)** toy experiments were made. For each experiment, the variable μ_0 was set between 0 and 1000, which is its typical range in the histograms to be monitor, and μ_1 was set according to which bad cell hypothesis. For each experiment 500 value were determined around μ_1 with poison distribution for which the test statistic T was determined. The critical value for 99% efficiency is the value of 0.01-*percentile* of T distribution. The results obtained for T_{crit} were fit with second order polynomial as a function of μ_0 (eq. 2.4).

$$T_{\text{crit}} = a \cdot \mu_0^2 + b \cdot \mu_0 + c \quad (2.4)$$

The results of the determination of each T_{crit} for each set of toys for both bad cell hypothesis and the corresponding fits can be found on figure 2.5.

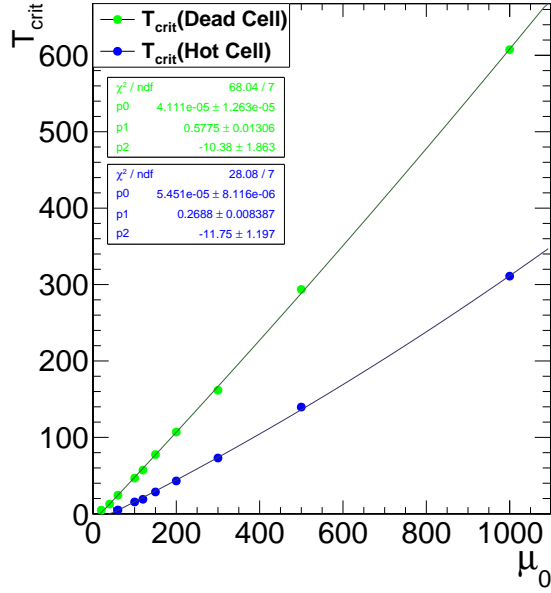


Figure 2.5: Graphic showing the results of the determination of T_{crit} as a function of μ_0 and the corresponding fit for each bad cell hypothesis. Results are for an efficiency of 99% and a fake rate of 1%.

To determine the minimum μ_0 and a function of the number of bins we need to fulfil both efficiency and fake rate conditions, this can also be determined with the help of MC. Searches for $\mu_{0\min}$ was preformed using an histograms with a predefined number of cells. For each tested μ_0 , five hundred experiments where made by filling all cells with a Poisoning random numbers around μ_0 . Resulting cells where then tested with T against the critical value determined for that specific μ_0 . The fake rate will be the fraction of experiments where one or more cells are marked as bad. The procedure is repeated for different μ_0 until the minimum value for this variable is found that exhibits a fake rate of 0.01 or lower. The procedure was repeated for the number of cells of all histograms to be initial monitored by this tool. The obtained values of μ_0^{\min} were fitted with a logarithm function as showed in equation 2.5.

$$\mu_0^{\min} = a \cdot \ln(b \cdot n_{\text{Bins}} + c) + d \quad (2.5)$$

On figure 2.6, all the calculated μ_0^{\min} values and the corresponding fits for both bad cell hypotheses tests are showed.

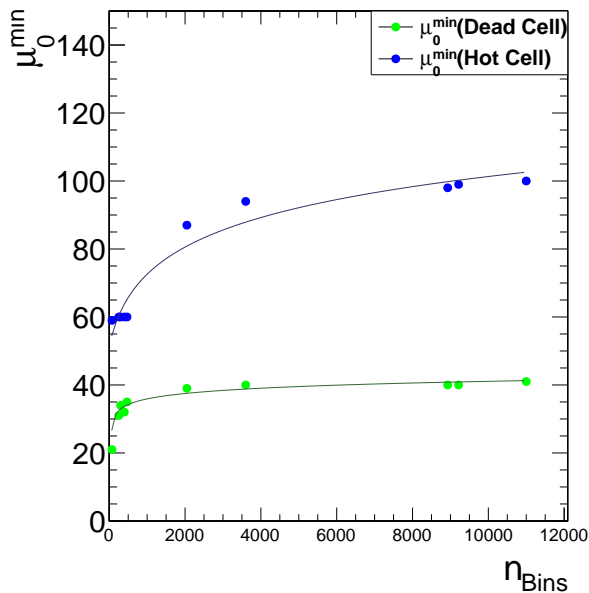


Figure 2.6: Graphic showing the results of μ_0^{\min} as a function of the number of bins and the corresponding fit for each bad cell hypothesis. Results are for an efficiency of 99% with a fake rate of 1%.

Implemented monitoring tool

The L1T occupancy monitor integrates the histograms in blocks of luminosity sections to ensure they have enough statistics. At the end of each luminosity section, with the help of the fits obtained in the previously, each strip of cell median is tested against the histograms μ_0^{\min} for both bad cell hypothesis tests. Cell and strips that are masked are ignored. If all strips have enough statistics the bad cell tests are performed and all cells that fail are marked as bad for the period of integration of the histogram. An example of an histograms integrated for a few luminosity sections and the results of the bad cell search are showed in figure 2.7.

An additional plot is produced for each one of the monitored histograms showing the fraction of unmasked cells that pass both bad cell tests. Automatic tests are attached to this histograms and are configured to flag as bad the luminosity sections that show more than 30% bad cells. This value is too high but was set in order to allow testing the full implementation of the tool and not to flag luminosity sections as bad while some of the original plots need intervention by the subsystem experts.

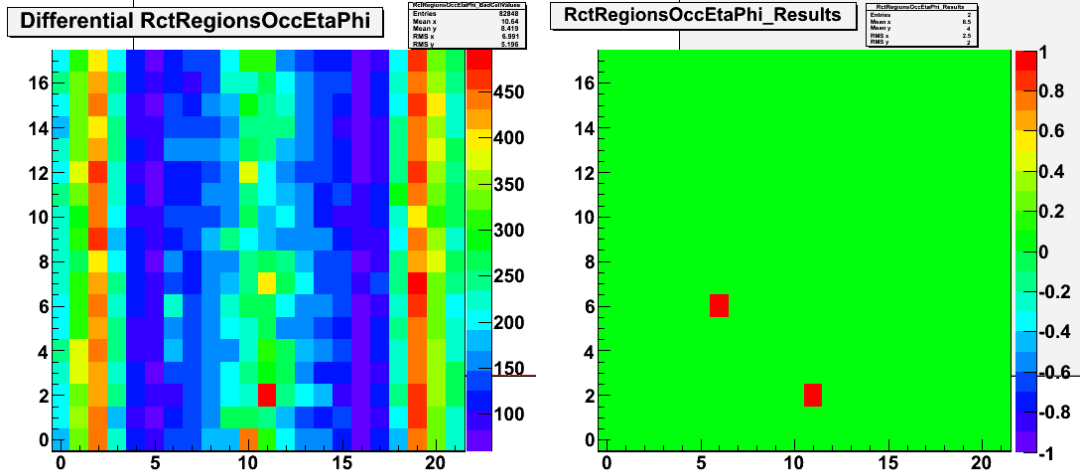


Figure 2.7: Monitoring plot produced by the [L1T](#) occupancy monitoring tool for run 207099 while testing [Global Calorimeter Trigger \(GCT\)](#) plot for isolated [Electromagnetic \(EM\)](#) region occupancy in $\eta - \phi$. On the left is the histogram under test which have been integrated for enough luminosity sections for meaningful results. On the right is an histogram where the cells that have passed the test are marked in green and red for the cells that failed. Two cells were found that fail the preformed tests.

2.3 Tests Summary

To simplify the task of the shift crew and certification for physics analysis an tests summary application was developed. This tool collects the results of other tests and presents them in a single set of plots as a function of the luminosity section. Three plots are produced, summaries of the [L1T](#) rates and [L1T](#) synchronization monitoring tools, and a global tests summary. In each histogram, the bottom horizontal line is the summary of the lines above, which is marked as bad (red) if any of the tests above fails. This scheme allows the user to quickly identify a problem by back tracing information from what tests where marked as bad starting from the summary line on the *L1T Tests Summary* histogram. An example of plots produced by this application can be found in figure 2.8.

The [L1T](#) occupancy monitoring was executed over histograms produced by other developers. Some of this histograms suffered from pathological problems that needs intervention from their authors. This caused the summary from that monitoring tool to always be flagged as bad. Although implemented, in order to avoid confusion it was decided to not enable this summary plot or add its results to the global summary until necessary changes to the original histograms are made.

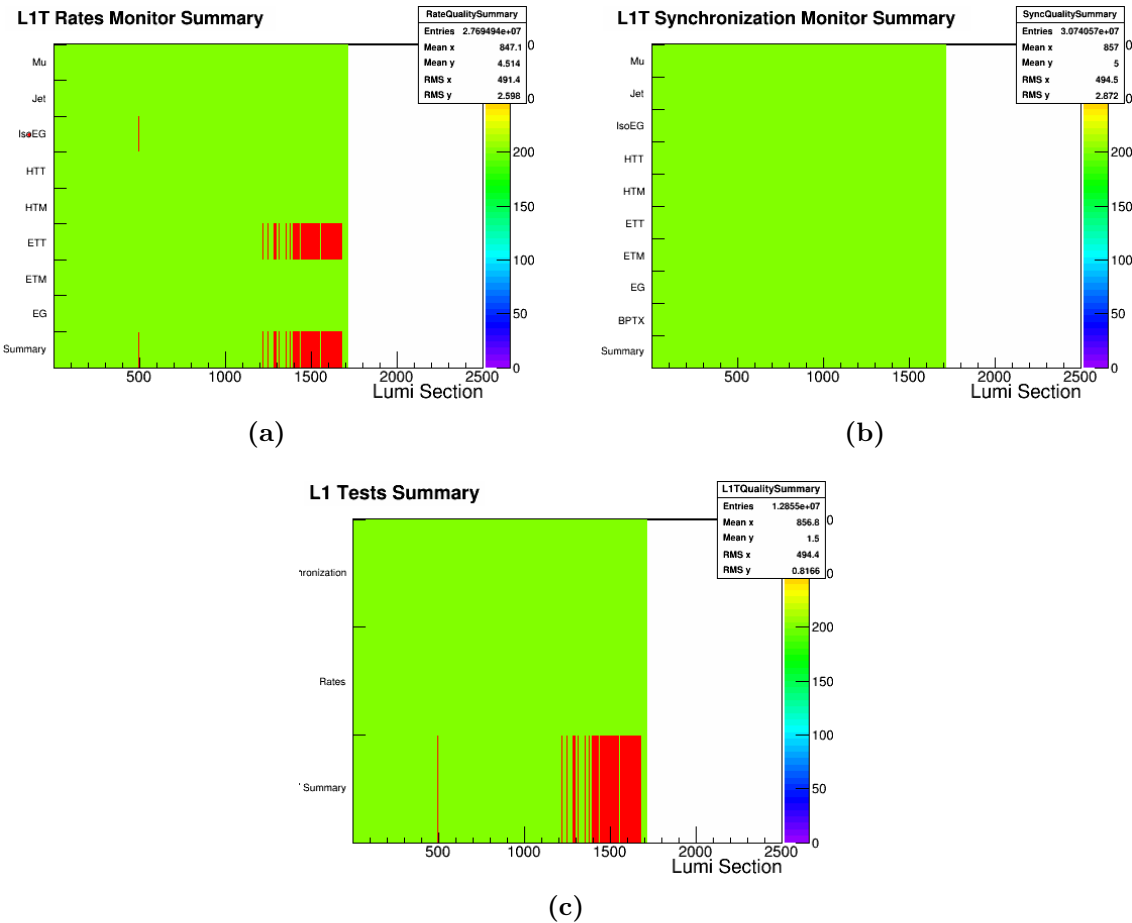


Figure 2.8: Example of the plots produced by the L1T test summary monitor. Figure (a) summary of all tests made by L1T rates monitor. Figure (b) summary of all tests made by L1T synchronization monitor, Figure (c) global summary of all tests performed.

Chapter 3

Event Reconstruction and simulation

This chapter describes how the **Compact Muon Solenoid (CMS)** detector produces physics objects from the information collected at each event. The **Vector Boson Fusion (VBF)** Higgs to invisible analysis uses almost all the physics objects reconstructed by the detector with making use of information from all the experiment sub-detectors. The following sections describe in detail each of these objects how they are reconstructed and what are the choices made to filter them. The last section describes how **Monte Carlo (MC)** methods are used to simulate physics processes and emulate the detector response.

3.1 Tracks

Reconstructing the trajectories of charged particles allows us to measure their momentum and determining their charge. This is possible by analysing the hit patterns in the inner tracking system. In **CMS** this reconstruction is made with the **Combinatorial Track Finder (CTF)** algorithm [33]. The relevant steps for track generation are described below:

- Seed generation is made with hits at the pixel detector. A track seeds can be made with two or three hits. In the first case a known vertex or the beam spot is used to constrain the seed momentum. The parameters of each seed are estimated using the assumption that the trajectory is a helix, but it takes into account hit errors and multiple scattering [34].
- The track seed is extrapolated through the tracker layers with a combinatorial Kalman filter [35]. For each additional layer, the best matching hit if any is added

and track parameters are recomputed. This procedure continues until the last layer is reached [33].

- Ambiguity resolution may be necessary since it is possible to have the same track being reconstructed from different seeds, or a seed may result in more than a single trajectory candidate. To resolve this possible double counting, when considering a pair of tracks with more than 50% of shared hits, we discard the one with the fewer amount of hits. In case of equal number of hits the one with lowest χ^2 is kept.
- After the track building and cleaning stages are done final refitting is performed. This procedure is aimed at removing possible bias by constraints at the seed forming stage. A standard Kalman filter and smoother are used.

The process of track finding is repeated up to six times where the hits for each successfully reconstructed track are removed for the next iteration. Using early Large Hadron Collider (LHC) data and a dataset of pions and muons it was possible to estimate that the tracking efficiency is $> 98\%$ for all track $p_T > 500 \text{ MeV}$ and $> 99\%$ for tracks with $p_T > 2, \text{ GeV}$ [36].

3.2 Vertex Reconstruction

The LHC can produce extreme collision intensities which are obtained partially by having multiple collisions happening at each bunch crossing. As it has been discussed in section 1.1.1 an average of 21 simultaneous collisions happened per bunch crossing in the CMS experiment during 2012. In this environment, it is crucial to identify the Primary Vertex (PV) and the particles that come from it. This information can then be used to reject particles coming from other additional collisions and to identify displaced vertices which can be the signature of long lived particles like b-mesons.

The individual tracks are reconstructed making use of the inner tracker. Each vertex is initially seeded by two tracks with separation in z less than 1 cm. Then remaining track are clustered to the vertex seeds with the Deterministic Annealing (DA) algorithm [37]. After the clustering process is done, the position of each vertex is recomputed using the Adaptive Vertex Fitter (AVF) algorithm [38]. In this algorithm weights, w_i are assigned to each track according to how compatible they are with the fitted vertex position. Weight vary from 1 to 0, being that track assigned weights of close 1 are highly

compatible with the vertex and close 0 would be given to low compatibility tracks. Then we can define the number of degrees of freedom of the new fit as:

$$n_{dof}(\text{vertex}) = 2 \sum_i^{\text{tracks}} w_i - 3 \quad (3.1)$$

This variable can be used to distinguish real proton-proton interactions from misclustered vertices, since it is correlated with the number of tracks compatible with that specific vertex [39]. The vertex position and resolution have been measured with LHC data and compared with simulation. The resulting plots can be found in figure 3.1 as a function of number of tracks.

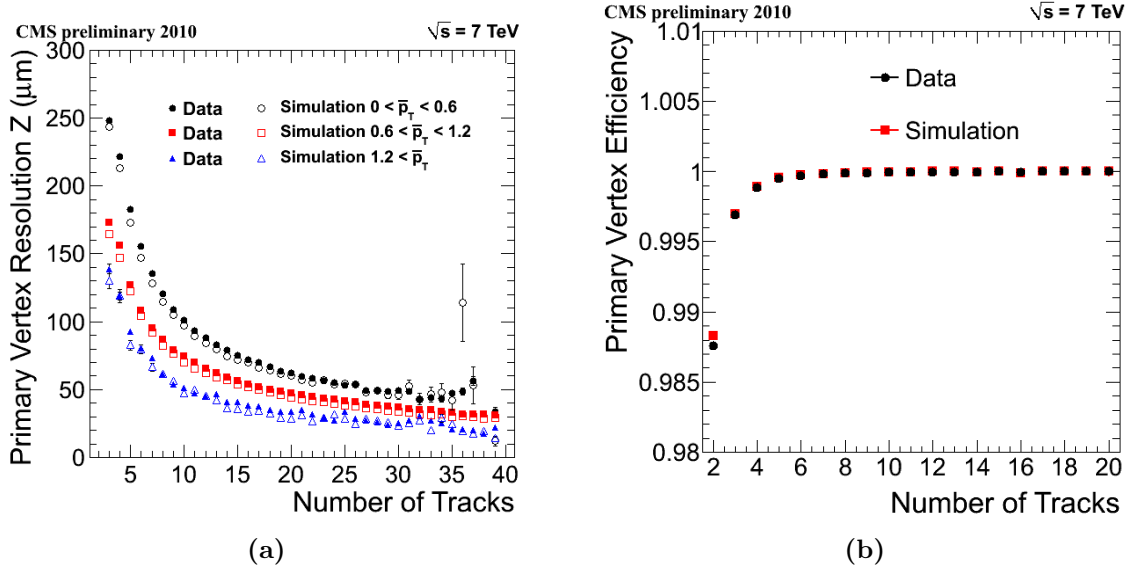


Figure 3.1: (a) Primary vertex resolution in the z coordinate as function of the number of associated tracks. Results are give for three ranges of average track p_T . (b) Primary vertex efficiency as a function of the number of associated track [39]

The PV is defined as the vertex with highest sum of associated tracks p_T squared. In situations where no vertex can be reconstructed, like if there is a tracking failure, the beam spot position is assumed. Knowing precisely the interaction point allows to determine particle candidate quantities relative to it which allow for better object identification and pile-up control.

Most CMS analysis, including the ones presented in this thesis, require explicitly that a good vertex is reconstructed with the following characteristics:

- Real reconstructed vertex from tracks, not the beam spot.
- A minimum number of degrees of freedom: $n_{dof} > 4$.
- Collision must be near the interaction region. We require longitudinal distance to be $|z| \leq 24$ cm (longitudinal impact parameter).
- Collision must be close to the beam line. Radial distance to beam line: $d_{xy} < 2$ cm (transverse impact parameter).

3.3 Particle Flow

The **Particle Flow (PF)** algorithm [40–42] is used in the **CMS** experiment with the objective of reconstructing every stable particle produced in the event. This is achieved by combining information from all **CMS** sub-detectors in order to identify electrons, photons, muons, charged hadrons and neutral hadrons and measure their direction, energy and type. The identified particles can in turn be used in jet clustering, determining the missing transverse energy, reconstructing and identifying taus, calculating particle isolation, identifying b-quark jets, etc.

The **CMS** experiment is very well suited for this approach since it is equipped with a high precision silicon tracker which is immersed in uniform axial magnetic field and its dual calorimeter design with high hermeticity and resolution. The tracker system allows very precise direction/momenta reconstruction for charged particles, down to transverse momentum as low as 150 MeV. The high granularity of the **Electromagnetic Calorimeter (ECAL)** allows for photons to be identified through deposit separation even inside high energy jets. In turn electrons can be reconstructed by combining their track and the energy deposits of the electron itself and its emissions, this algorithm will be explained further in section 3.4. The tracker information also allows to separate charged and neutral hadrons in close proximity, a task which is not possible with just the **Hadronic Calorimeter (HCAL)** due to its coarser granularity. We can determine the charged hadron momentum from the track information, and then, by removing its deposit from the calorimeter system we can determine the neutral hadron deposits. In areas outside the tracker and/or **ECAL** coverage, measurements are more coarse since we have less information available.

The clustering is performed separately in the **ECAL** and **HCAL** algorithm. We start by identifying *seed clusters* which are local maxima of calorimeter cell energy deposits. We

add neighbouring cell into *topological clusters* if their energy deposit is bigger than two standard deviations of the electronics noise. This value was determined to be 80 MeV for the **ECAL** barrel, up to 300 MeV for the **ECAL** endcap and 800 MeV for the **HCAL**. The energy of each cell may be shared between multiple clusters.

Tracks and clusters are **PF** elements that need to be linked together to reconstruct the particle they came from and also to avoid double counting. We pair elements based on a metric of distance between elements and if compatible we merge them into *blocks* which can interpreted as particle candidates. As an example, a pair of a track and energy cluster on the calorimeter system would be linked if you could extrapolate the track to the cluster volume.

3.3.1 Isolation

To reduce the probability of misidentification of a lepton coming from **Quantum Chromodynamics (QCD)** jets as opposed to one coming from the hard scattering we can require isolation [43, 44]. We compute the isolation by summing the transverse momenta of all particles inside a cone around the selected lepton. In this sum we include all charged particles, neutral hadrons and photons. But we do not want to include the **Pile-Up (PU)** contribution to this sum so we only include the charged candidates with an impact parameter smaller than 0.1 cm. Different methods are used for each particle to estimate and subtract the neutral component of the **PU** depending on **Particle Object Group (POG)** recommendations.

Normally, for physics analysis we defined the more meaningful *relative isolation* as $I_{rel} = I/p_T^{lepton}$. By using, a quantity that is relative to the the candidate p_T and not an absolute cut we avoid wrongly accepting low energy candidates or rejecting an high energy candidates. In the next sections the steps taken to calculate this quantity for each particle candidate are explained.

3.4 Electrons

In the **CMS** experiment electrons are reconstructed by matching energy clusters in the **ECAL** with tracks coming from the inner tracking system. Unfortunately, electrons can loose and disperse significant amounts of energy until they reach the **ECAL**. While they transverse the inner tracker they may emit photons through bremsstrahlung and in turn

these photon can convert to e^+e^- pairs. About 35% of the electron radiate at least 70% of their energy in this way [45]. This spread of energy is mostly in ϕ due to the applied magnetic field [46]. Dedicated algorithms were developed to combine the the ECAL energy deposits, into a so called *supercluster*, of the initial electron and its emissions.

Different algorithms are used in the barrel and endcaps regions. In the barrel region we explore the simple $\eta - \phi$ geometry with the *hybrid clustering algorithm*. The procedure starts by identifying *seed crystals* with $E_T > 1\text{ GeV}$. A domino shaped cluster is formed around this seed in the η direction of 3×1 or 5×1 crystals centred at the seed. Additional dominoes are added in both ϕ direction in an attempt to collect the bremsstrahlung emissions up to $\Delta\phi \approx 0.3\text{ rad}$. Any domino with energy below 100 MeV is disregarded. The resulting additional sub-clusters must have its own seed with $E_T > 350\text{ MeV}$ and they are all combined to form the final *supercluster*.

In the endcaps the *Multi-5 \times 5 algorithm* is used. In this region of the detector the geometry is more complex and does not follow a simple $\eta - \phi$ symmetry. The seeds for the this clustering procedure are the crystals which are local maxima over their four direct neighbours and have a deposit of $E_T > 0.18\text{ GeV}$. Then, and starting with the seeds with highest E_T , we collect the energy around them into clusters of 5×5 crystals. We then search for similar seeds and form clusters that can overlap within $\Delta\eta < 0.07$ and $\Delta\phi < 0.3\text{ rad}$ of the initial seed. Those clusters are then combined into a single *supercluster* which needs to have at least $E_T > 1\text{ GeV}$. The *supercluster* is then extrapolated to the ECAL preshower by clustering the energy within $\Delta\eta < 0.15$ and $\Delta\phi < 0.45$ around the most energetic cluster and adding it to the *supercluster* itself [43].

In order to reconstruct the electron track we need to take into account the bremsstrahlung emissions. The CTF algorithm is not appropriate for this purpose so a different track-finding algorithm had to be developed. For high p_T electrons we use the ECAL supercluster energy deposit weighted mean impact point as a seed. If we combine this information with the determined E_T we can define two $\eta - \phi$ search regions in the pixel detector depending on the charge hypothesis. If we find two compatible hits, the electron trajectory is updated. From this point normal track building is performed but instead of a Kalman filter algorithm we use a Gaussian Sum Filter (GSF) algorithm [47]. This method performs better in the presence of non-Gaussian losses like the one coming from the bremsstrahlung emissions.

The typical background to real electrons are collimated hadronic jets, like from π^0 and π^\pm overlap or from π^\pm showers [45]. There are many useful variables that may be used to reduce such background and are often used in *electron identification* criteria:

- $\Delta\eta_{in}$ and $\Delta\phi_{in}$, are the distance between the track direction at the vertex and extrapolated to the ECAL and supercluster.
- $\sigma_{i\eta i\eta}$ is the energy-weighted η width of the cluster. For real prompt electrons this is normally small since this quantity is not significantly affected by the magnetic field.
- H/E is the ration of hadronic to electromagnetic energy in the region of the seed cluster.

Distributions of these variables for simulated electrons and jets can be found in figure 3.2.

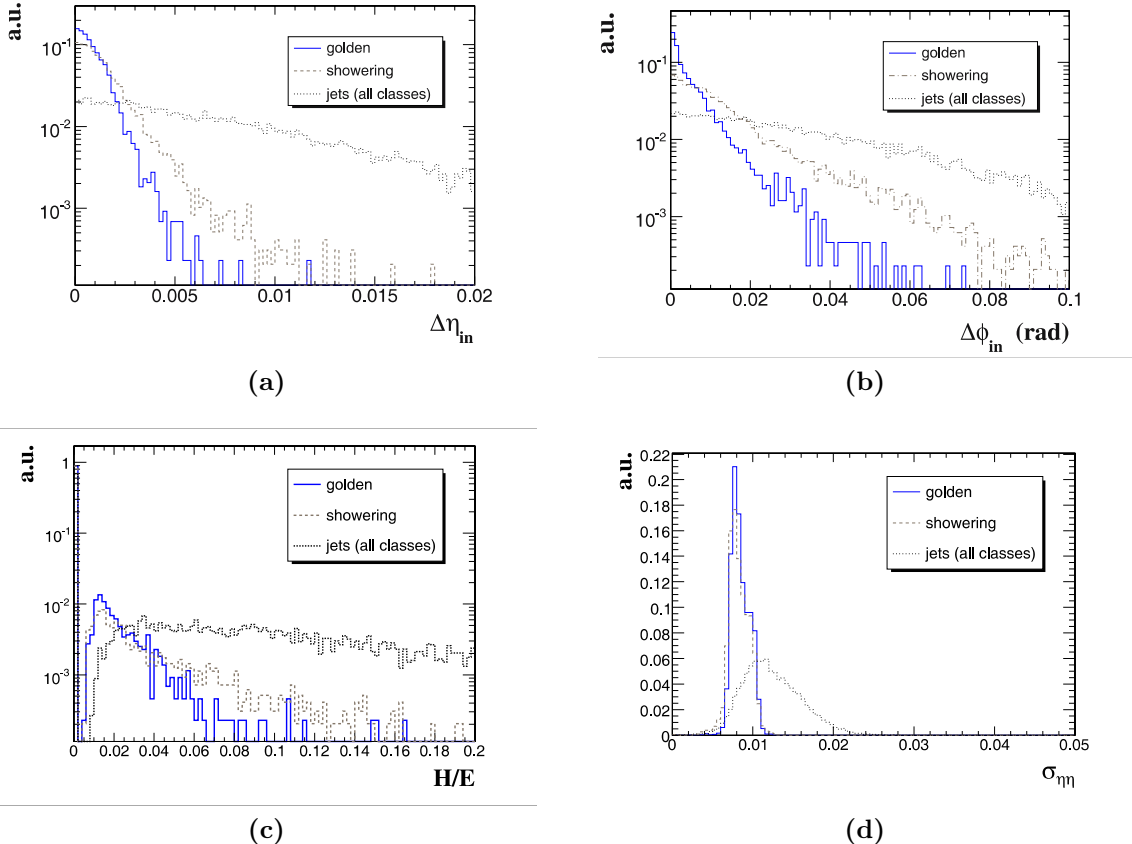


Figure 3.2: Distributions for (a) $\Delta\eta_{in}$, (b) $\Delta\phi_{in}$, (c) H/E and (d) $\sigma_{i\eta i\eta}$. Here *golden electrons* are those who emit minimal bremmstrahlung photons, *showering* are electrons that lose a large fraction of their energy in emissions and *jets* are the typical distributions for hadronic jets. [45]

3.4.1 Isolation

For electrons we calculate isolation with the *effective area corrected isolation* method over a cone of $\Delta R < 0.3$ around the electron. For the neutral PU subtraction we uses a look-up table of effective areas according to electron $|\eta|$ which is multiplied by the estimated neutral PU energy density by unit of effective area. The definition for this isolation can be found in equation 3.2.

$$I = \sum_{\text{charged non-pileup}} p_T + \max \left(0, \sum_{\text{neutral}} p_T + \sum_{\text{photon}} p_T - \rho(\text{lepton}) \times \text{Eff. Area}(\text{lepton}) \right) \quad (3.2)$$

3.4.2 Veto electrons

We define *veto electrons* as an electron candidate with $p_T > 10 \text{ GeV}$ and $|\eta| < 2.4$ which passes the CMS Electron/Gamma POG [48] requirements of the cut based electron Identification (ID) *veto electron* working point. A summary of these conditions can be found in table 3.1.

Variable	Barel	Endcap
$ \Delta\eta(\text{track}, \text{supercluster}) $	< 0.007	< 0.1
$ \Delta\phi(\text{track}, \text{supercluster}) $	< 0.8	< 0.7
$\sigma(i\eta, i\eta)$	< 0.01	< 0.03
H/E	< 0.15	-
$ d_0(\text{vertex}) $	< 0.04	< 0.04
$ d_Z(\text{vertex}) $	< 0.2	< 0.2
$\frac{PF_{isolation}}{p_\perp}$ for $\Delta R_{cone} = 0.3$	< 0.15	< 0.15

Table 3.1: Details of the CMS Electron-Gamma POG recommendations for a *veto electron*. Here barrel is defined as $|\eta_{\text{supercluster}}| \leq 1.479$ and endcap is $1.479 < |\eta_{\text{supercluster}}| < 2.5$.

3.4.3 Tight electrons

We also define *tight electrons* as an electron candidate with $p_T > 20 \text{ GeV}$ and $|\eta| < 2.4$ which passes the CMS Electron/Gamma POG requirements of the cut based electron ID

tight electron working point. This working point is similar to the 2011 very tight WP70 working point. A summary of these conditions can be found in table 3.2.

Variable $p_T > 20 (p_T \leq 20)$	Barel	Endcap
$ \Delta\eta(\text{track}, \text{supercluster}) $	< 0.004	< 0.005
$ \Delta\phi(\text{track}, \text{supercluster}) $	< 0.3	< 0.2
$\sigma(i\eta, i\eta)$	< 0.01	< 0.03
H/E	< 0.12	< 0.10
$ d_0(\text{vertex}) $	< 0.02 cm	
$ d_Z(\text{vertex}) $	< 0.1 cm	
$ \frac{1}{E} - \frac{1}{p} $	< 0.05	
$\frac{PF_{isolation}}{p_\perp}$ for $\Delta R_{cone} = 0.3$	< 0.10	< 0.10(0.07)
Conversion rejection: vertex fit probability	$< 1 \times 10^6$	
Conversion rejection: missing hits	= 0	

Table 3.2: Details of the CMS Electron-Gamma POG recommendations for a *tight electron*. Here barrel is defined as $|\eta_{\text{supercluster}}| \leq 1.479$ and endcap is $1.479 < |\eta_{\text{supercluster}}| < 2.5$.

3.5 Muons

Muon track reconstruction starts independently at the inner-tracker (*tracker track*) and in the muon systems (*standalone muon track*) [44]. Then this information can be combined into a single muon track in two possible ways.

Global Muon reconstruction is an *outside-in algorithm*. We start by finding tracker track match for each standalone muon track. This is done by propagating the match candidate pair to a common surface and comparing track parameters. For each matched pair, a *global-muon fit* is performed using all hits from the two tracks using a Kalman-filter algorithm [35]. For muons of $p_T \gtrsim 200 \text{ GeV}/c$, it has been showed that a *global-muon fit* improves the momentum resolution compared to a *tracker-only fit* [10, 49].

Tracker Muon reconstruction is an *inside-out algorithm*. In this method we start by selecting all tracker tracks with $p_T > 0.5 \text{ GeV}$ and $p > 2.5 \text{ GeV}$. We extrapolate those tracks to the muon system while taking into account the magnetic field, energy loss and scattering. If we find a match with at least one muon segment in the muon system (track

stub in the Drift Tube (DT) or Cathode Strip Chamber (CSC)) this tracker track now becomes a Tracker Muon.

Tracker muon reconstructions is more efficient than the global muon reconstruction at low momenta at $p \lesssim 5 \text{ GeV}$. This difference is due to tracker muons reconstruction only requiring one segment on the muon system. While global muon reconstruction is more efficient for higher energies where the muons are more likely to pass several muon stations.

Muons can be also be classified as prompt or non-prompt. The prompt muons are the ones produced directly in the hard process like the decays of vector bosons or quarkonia particle decays. On the other hand, non-prompt muons typically come from in-flight decays of light hadrons, from taus or heavy quark decays.

When reconstructing global muons, it's unlikely to find non-prompt muons but we may have hadronic activity “punching-through” the calorimeter system and appearing in the muon system. To reduce this types of background we can use different muon identification criteria.

Studies with the CMS detector have been performed to asses muon reconstruction efficiency [44]. Muon was defined as candidate with global fit track using tracker and muon chamber hits with a χ^2 per degree of freedom of less than 10. This fit must include at least one segment in the muon chamber, track segments in at least 2 muon stations, use more than 10 hits in the inner tracker of which at least one in the a pixel layer and finally a small transverse impact parameter $|d_{xy}| < 2 \text{ mm}$. The efficiency for such a criteria has been measured both in data and Monte Carlo using $J/\psi \rightarrow \mu^+ \mu^-$ and $Z \rightarrow \mu^+ \mu^-$ and for $p_T > 10 \text{ GeV}$ it plateaus at 96-99%.

3.5.1 Isolation

For muons we use the *combined isolation* over a cone of $\Delta R < 0.4$ around the muon. For neutral PU subtraction we use the charged PU component inside the cone and multiply it by a factor of 0.5 which is determined from simulation. The definition for this isolation can be found in equation 3.3.

$$I = \sum_{\text{charged non-pileup}} p_T + \max \left(0, \sum_{\text{neutral}} p_T + \sum_{\text{photon}} p_T - \frac{1}{2} \sum_{\text{charged pileup}} p_T \right) \quad (3.3)$$

3.5.2 Loose Muons

We can define *loose muon* using the cut based definitions recommend by the CMS Muon POG [50] with the same name, where we require the muon candidate to be a PF muon which is also a tracker or global muon. We exclude only standalone muons which are only $\approx 0.01\%$ of the PF muons. Additionally we require the muon candidate to have $p_T > 10 \text{ GeV}$, $|\eta| < 2.1$ and relative combined isolation < 0.2 .

3.5.3 Tight Muons

We can also define *tight muon* as a muon candidate with $p_T > 20 \text{ GeV}$, $|\eta| < 2.1$ passing relative combined isolation < 0.12 . Additionally, we require compatibility of being produced at the primary vertex by requiring $d_{xy} < 0.045 \text{ cm}$ and $d_z < 0.2 \text{ cm}$. We also require the muon to pass the CMS Muon POG recommended cut based *tight muon* identification criteria that requires the candidate to be a PF muon which is also a global muon. Where the the global track fit has at least one muon chamber hit and $\chi^2/ndof < 10$. The presence of muon segments in at least two chambers, at least five tracker layers with hits and at least one pixel hit.

3.6 Jets

When we collide hadrons the most probable hard processes will be the scattering quarks and gluons. However, these do not reach our detectors. They quickly hadronize and fragment generating a collimated spray of particles which is commonly referrer to as a jet. To determine the properties of this outgoing quarks and gluons we need therefore to look at the characteristics of their associated jets. To achieve this goal we need to combine the measured jet remnants in a way that preserves the physical properties of the original parton.

3.6.1 Jet Clustering

Jet clustering algorithms are sets of rules that allows us to combine particle candidates into a jets [51]. These algorithms normally are controlled by parameters that define how close particles need to be in order to be associated into a jet and a way to combine their momentum. However, a jet definition should be robust and provide consistent measurements about the parton. There are two major families of problems that may affect a jet algorithms. These problems appear when the number of jets in an event changes by adding a soft collinear gluon emissions (collinear safety) or by parton splitting (infrared safety).

In CMS we use a sequential recombination algorithm known as anti- k_T [52] which is both infrared and collinear safe. This algorithm starts by determining a measurement of distance between every pair of objects d_{ij} and a the distance of each object to the beamline d_{iB} . The definition of these distances can be found in equations 3.4 and 3.5 respectively.

$$d_{ij} = \min(p_{T_i}^{2p}, p_{T_j}^{2p}) \frac{\Delta R_{ij}^2}{R^2} \quad (3.4)$$

$$d_{iB} = p_{T_i}^{2p} \quad (3.5)$$

Where ΔR is the separation the $\eta - \phi$ plane and R is the maximum diameter for the jet. The parameter p determines the type of algorithm. When p equal to 1 its a k_T algorithm, 0 for the Cambridge/Aachen algorithm and -1 for the anti- k_T .

After determining all the d_{ij} and d_{iB} we determine which is the minimum distance. If it is a d_{ij} we combine those two object and recalculate all the distances. If the minimum is a d_{iB} we declare i to be a *final state jet*, and remove it from the list of particles and recalculate all distances the again. The procedure continues until there are no more objects remaining.

The anti- k_T algorithm tend to cluster particles around a the hardest particle in a region which normally leads to a cone like jet area in the $\eta - \phi$ plane. In the VBF Higgs to invisible analysis the clustering is made over PF particle candidates using the implementation in the FASTJET software package [53]. The CMS recommended cone diameter size for 2012-13 analysis is of 0.5 while for 2015 is of 0.4.

3.6.2 Particle Flow Jet Identification

The CMS Jet-MET POG has defined criteria to reject fake, badly reconstructed, and noisy PF jets while keeping 98-99% real jets. All the presented analysis in this thesis we have used the recommended PF jet ID in the loose working point. In this working point all jets are required to have at least two constituents, and both neutral hadron fraction and a neutral Electromagnetic (EM) fraction to be below 99%. Additionally for jets inside the tracker acceptance with $|\eta| < 2.4$ we require the charged multiplicity and charged hadron fraction to be bigger than zero, and the charged EM fraction to be less than 99%.

3.6.3 Pileup Jet Identification

To identify if a PF jet has come from PU or from the primary vertex we make of a Boosted Decision Tree (BDT). This machine learning algorithm was trained with information about the trajectory of the tracks associated with the jet, the jet shape, and object multiplicity. In the presented analyses we have used the recommended loose working point of the *full BDT method*. This method was applied to each jet which would only be accepted if the BDT output score would pass the cuts defined in table 3.3 depending on jet p_T and η .

Jet p_T	Jet $ \eta $	BDT_{score}
$20 < p_T \leq 30$	$ \eta < 2.5$	> -0.80
$20 < p_T \leq 30$	$2.50 \leq \eta < 2.75$	> -0.85
$20 < p_T \leq 30$	$2.75 \leq \eta < 3.00$	> -0.84
$20 < p_T \leq 30$	$3.00 \leq \eta < 5.00$	> -0.85
$30 < p_T$	$ \eta < 2.5$	> -0.80
$30 < p_T$	$2.50 \leq \eta < 2.75$	> -0.74
$30 < p_T$	$2.75 \leq \eta < 3.00$	> -0.68
$30 < p_T$	$3.00 \leq \eta < 5.00$	> -0.77

Table 3.3: Table of the minimum values of *full BDT method* score for a PF jet to be accepted as coming from the PV using a loose working point. Required minimum values have been binned in jet p_T and η .

3.6.4 Lepton cleaning

To avoid having leptons being miss reconstructed as jets we filter out all jets which are located at $\Delta R < 0.5$ to any veto electron or loose muons.

3.6.5 Jet Energy Corrections

When reconstructing a jet the clustered energy often does not match the parton energy that gave it origin. There are many reason for this effect like non-linearity of the calorimeters response, detector noise, overlap with problematic detector areas, additional energy from PU, miss calibration, etc. To fix this problem corrections are determined and applied to each jet in order to in average have an energy measurements that is equal to the original hadron. This corrections can be factorized into components as it is represented in equation 3.6 [54].

$$P_{\text{corr}}^{\mu} = C_{\text{offset}}(p_T^{\text{raw}}, \eta) \cdot C_{\text{rel}}(p_T^{\text{off}}, \eta) \cdot C_{\text{abs}}(p_T^{\text{rel}}, \eta) \cdot P_{\text{raw}}^{\mu} \quad (3.6)$$

The C_{offset} term accounts for and subtracts the contribution of PU and noise in the detector measurements. Its value is determined by taking into account the specific event p_T -density expressed in the ρ variable, and the individual jet area A [55]. The event ρ is calculated as the median p_T -density of all jets present in the event. Since the median is taken it will not be affected by the presence of hard jets. Unfortunately, the Underlying Event (UE) activity has similar characteristic to the PU and should not be subtracted. To avoid this effect the correction takes the form of $\rho - \langle \rho \rangle_{\text{UE}} \cdot A$, where $\langle \rho \rangle_{\text{UE}}$ is the average expected UE contribution.

The C_{rel} term is applied to make the energy response flat as a function of η . It is applied to the offset corrected transverse momentum p_T^{off} . To determine its value the p_T -balancing method is used [54]. In this method we select a reference jet located in the central region where energy measurement is expected to be flat and a probe jet at any value of η . We can calculate the average of balance quantity as $(p_T^{\text{probe}} - p_T^{\text{reference}})/p_T^{\text{average}}$ which is used to determine the correction to response in bins of jet η and dijet average p_T .

The C_{abs} term is intended to make the response uniform in p_T . It is applies to the η corrected transverse momentum p_T^{rel} and is calculated using the Missing

Transverse Energy Projection Fraction (MPF) method [56]. In this method we use the good experimental resolution for leptons and photons in processes like $\gamma + \text{jets}$ and $Z + \text{jets}$ to infer on the properties of the recoil jets. Since these processes should not have Missing Transverse Energy (MET), if observed it can be used to calibrate the jet response for the jets present in the event.

The total uncertainty on the jet energy scale is obtained by summing in quadrature the estimated uncertainties of each one of the correction terms. The total uncertainty is in the range of $\approx 3 - 5\%$ depending on p_T and η [54].

3.7 Hadronic Taus

Taus can decay leptonically and hadronically. In leptonic decays the tau decays directly to an electron and two additional neutrinos. Therefore it is very difficult to identify such decays experimentally. On the other hand an hadronic tau decay produces a characteristic signature of a narrow jet containing an odd number of charged particles and additional neutral hadrons as well as a tau neutrino. In all the analysis presented in this thesis when referring to a tau we refer an hadronically decaying tau. The most probable decay modes have one or three charged π mesons and are summarized in table 3.4.

Decay Channel	Resonance	Mass [MeV]	Branching Fraction [%]
$\tau^\pm \rightarrow \pi^\pm \nu_\tau$			11.6
$\tau^\pm \rightarrow \pi^\pm \pi^0 \nu_\tau$	ρ	770	26.0
$\tau^\pm \rightarrow \pi^\pm \pi^0 \pi^0 \nu_\tau$	a_1	1260	10.8
$\tau^\pm \rightarrow \pi^\pm \pi^\mp \pi^\pm \nu_\tau$	a_1	1260	9.8
$\tau^\pm \rightarrow \pi^\pm \pi^\mp \pi^\pm \pi^0 \nu_\tau$			4.8
Other hadronic modes			1.7
Total			64.7

Table 3.4: Summary of the hadronic tau decay modes, with the branching fractions and intermediate resonances listed where relevant [57].

Reconstruction of hadronic tau neutrinos with PF is done by identifying the specific decay mode visible products. The approach is at the core of the Hadron Plus Stips (HPS) algorithm [58, 59]. It combines reconstructed charged hadrons with strips of clustered photons which are interpreted as π_0 . The reconstructed system is constrained by the tau

mass and intermediate resonances which results in a highly collimated jet when compared with a typical QCD jet.

3.7.1 Hadron Plus Stips Algorithm

The HPS algorithm utilizes PF candidates to reconstruct charged pions and photons resulting from neutral pions decay. These photon can convert in into electron-positron pairs in the tracker material. This factors are taken into consideration, as well as deflection in the magnetic field. We also attempt to find the intermediate resonances listed in table 3.4 has a handle to determine the tau decay channel. A tau neutrino is present on all decays and cannot be directly measured, this results in a smearing of the measured tau mass when considering only the visible products.

We seed the algorithm with PF anti- k_T jets with $R = 0.5$ where $p_T > 14 \text{ GeV}$ and $|\eta| < 2.5$. To search for the π^0 decay products we try to identify strips by clustering PF electrons and photons with $p_T > 0.5 \text{ GeV}$. We start from the most energetic electromagnetic particle inside the jet area and make that the centre of our candidate strip. We look for other electromagnetic objects within a window of $\Delta\eta = 0.05$ and $\Delta\phi = 0.20$ of the centre of the strip. If an object is found it gets associated with the strip and its four-momentum gets recalculated. We repeat the procedure until we cannot find any more unassociated EM objects inside the strip area. If the final strip object has a mass compatible with a π^0 , in the interval between $50 - 200 \text{ MeV}$, and has $p_T > 2.5 \text{ GeV}$ it is kept. We then start the next strip clustering with the highest p_T electron or gamma not already belonging to a strip.

The charged pion candidates are required to have $p_T > 0.5 \text{ GeV}$ and its track pass $d_z < 0.4 \text{ cm}$ and $d_{xy} < 0.03 \text{ cm}$ to the vertex associated with the highest p_T track in the jet, which is assumed to be the τ production vertex.

The following topologies are taken into account by the HPS algorithm:

1. *single hadron*: tries to identify tau decays into $\pi^\pm \nu_\tau$ or $\pi^\pm \pi^0 \nu_\tau$ where the netral pion decay cannot be identified as a strips.
2. *One hadron + one strip*: tries to identify tau decays into $\pi^\pm \pi^0 \nu_\tau$ where the π^0 decay photons are close together. In this case we are selecting the $\rho(770)$ intermediate resonance. The mass of the reconstructed τ_{had} is required to be in the interval $0.4 < m_{\tau_{had}} < 1.3 \text{ GeV}$ for $p_T^{\tau_{had}} < 200 \text{ GeV}$. The upper limit in the mass window

can go up to 2.1 GeV for candidates with $p_T^{\tau_{had}} > 200$ GeV to account for resolution effects.

3. *One hadron + two strip*: tries to identify tau decays into $\pi^\pm \pi^0 \nu_\tau$. In this case we are selecting the $a_1(1260)$ intermediate resonance. The mass of the reconstructed τ_{had} is required to be in the interval $0.4 < m_{\tau_{had}} < 1.2$ GeV for $p_T^{\tau_{had}} < 200$ GeV. The upper limit in the mass window can go up to 2.0 GeV if the $p_T^{\tau_{had}}$ increases above 200 GeV.
4. *Three hadrons*: tries to identify tau decays into $\pi^\pm \pi^\mp \pi^\pm \nu_\tau$. The hadrons are required to have mass in the interval $0.8 - 1.5$ GeV since we assume the $a_1(1260)$ intermediate resonance. Total charged is required to be one.

There is no dedicated search for $\pi^\pm \pi^\mp \pi^\pm \pi^0 \nu_\tau$ or higher pion multiplicity decay modes. These topologies are reconstructed with the currently defined criteria.

All selected hadrons and strips are required to be inside of cone of $\Delta R < 2.8$ GeV/ $p_T^{\tau_{had}}$. The cone size is constrained to the interval $\Delta R = 0.05 - 0.10$.

3.7.2 Isolation and Discriminants

Isolation for taus is calculated in a similar way to electrons and muons. The isolation variable is defined by summing the p_T of all **PF** hadron and photon candidates in a cone of $\Delta R < 0.5$ around the tau axis. Here the charged hadron tracks are required to have $d_z < 2$ cm to the tau production vertex. We can subtract the contribution to isolation coming from **PU** estimating its density in a cone of $\Delta R < 0.8$ around the tau and considering track with $d_z > 2$ cm. All tau constituents are ignored in this sums. Working points have been defined for loose, medium and tight isolation [59].

Electrons can be reconstructed as taus when they make isolated deposits in the calorimeter or emit enough energy via bremsstrahlung to form a strip. A **BDT** has been trained with a set of variables similar to the ones used in electron identification to exclude such miss reconstructions. Similarly to isolation three working points have been defined [58, 59].

Muons are less likely to be reconstructed as a tau. We can exclude such tau candidates by requiring that the track of the leading charged hadron is not also a tracker muon. This discriminator also has three possible working points [58, 59].

We can now define an hadronic tau candidate as a **PF** tau candidates with $p_T > 20$ GeV, $|\eta| < 2.3$ and $d_z < 0.2$ cm to the primary vertex. We require that the candidate passes

decay-mode identification, tight isolation and finally tight discriminators against electrons and muons.

3.8 Missing Transverse Energy

The Standard Model describes neutrinos as particles which only interact via the weak force. They can pass through our detectors without interacting and therefore not allowing any direct measurement. Many new models describe additional particles that would also be able to escape detection by leaving very small or no energy deposits in our experiments. The appearance of such particles can only be inferred through the measurement of an imbalance of transverse momentum of all detected particles. These effect can be quantified as the negative sum off all visible particle candidates transverse momentum in an event.

The magnitude of that vector is referred to as **Missing Transverse Energy (MET)**. Particle flow methodology provides a complete list of objects candidates in the event with excellent resolution achieved by combining all available information. Making it well suited to be the input for **MET** calculation. Although **CMS** has an excellent individual particle resolution the calculation of **MET** is affected by the combined resolution of the measurement of all particles in the event. Figure 3.3 shows the distributions of **PF MET** for both data and simulation for event selections of $Z \rightarrow \mu\mu$ and $\gamma + jets$ processes at $\sqrt{s} = 8 \text{ TeV}$.

Both photons and muons energy measurements have good resolution in the **CMS** experiment and these processes do not involve real **MET**. The observed distribution in both plots are predominantly shaped by the energy resolution of jet energy measurement.

During data taking issues with the detector or data acquisition can happen creating anomalously high **MET** and rendering this events unusable. The groups responsible for each part of the detector and individual physics objects, check the data after it was taken to find if such problems have occurred. After this problems are identified they produce software event filters for analysts to be able to remove this problematic events. The **CMS JET-MET POG** compiled a list of the recommended filters for analysis using 2012-13 data to remove events affected by energy deposits from beam halo, noise in **HCAL** readout electronics, particles directly hitting the **ECAL** photodiodes, track reconstruction problems and finally **ECAL** and **HCAL** miss timed laser calibration sequence. This filters have been used in both prompt and parked **VBF** Higgs to invisible analyses.

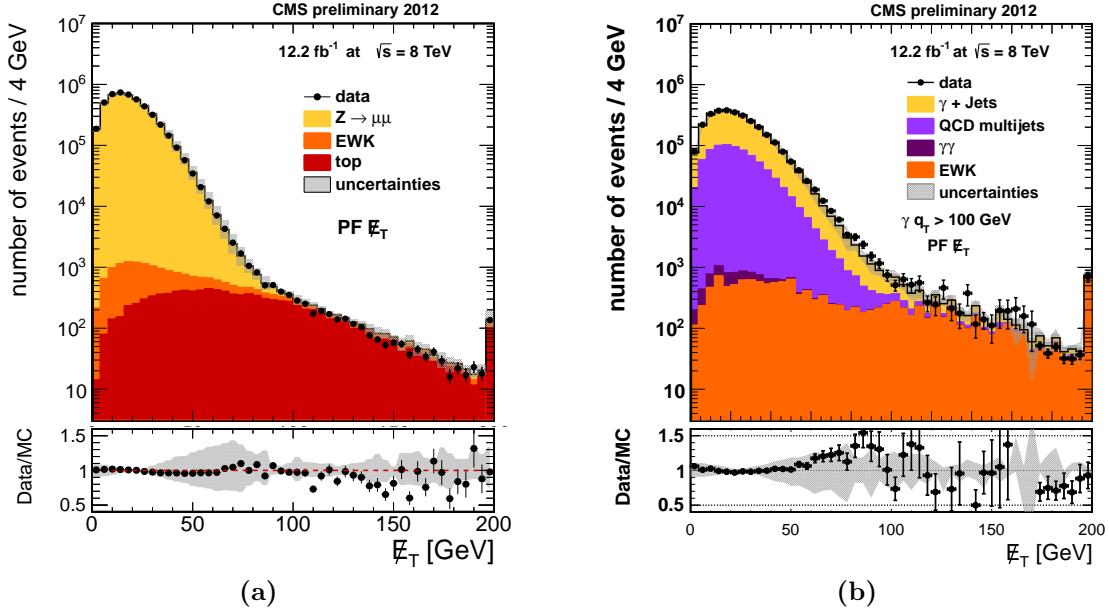


Figure 3.3: Distributions of the particle flow E_T^{miss} in a) $Z \rightarrow \gamma\gamma$ and b) $\gamma + \text{jets}$ events in $\sqrt{s} = 8 \text{ TeV}$ data and simulation. The uncertainty in the muon, photon, jet and neutral hadron energy responses is showed by the shaded band [60].

There are many factors that affect **MET** response and resolution. These include zero suppression thresholds which dictate the minimum energy a calorimeter cell will report, dead or non-instrumented regions of the detector and reconstruction inefficiencies. Techniques have been developed to correct both response and resolution when using **PF MET** [61]. These corrections include accounting for the bias in response due to using incorrect energy scale of the jets, and reducing the impact of pileup on the resolution [60].

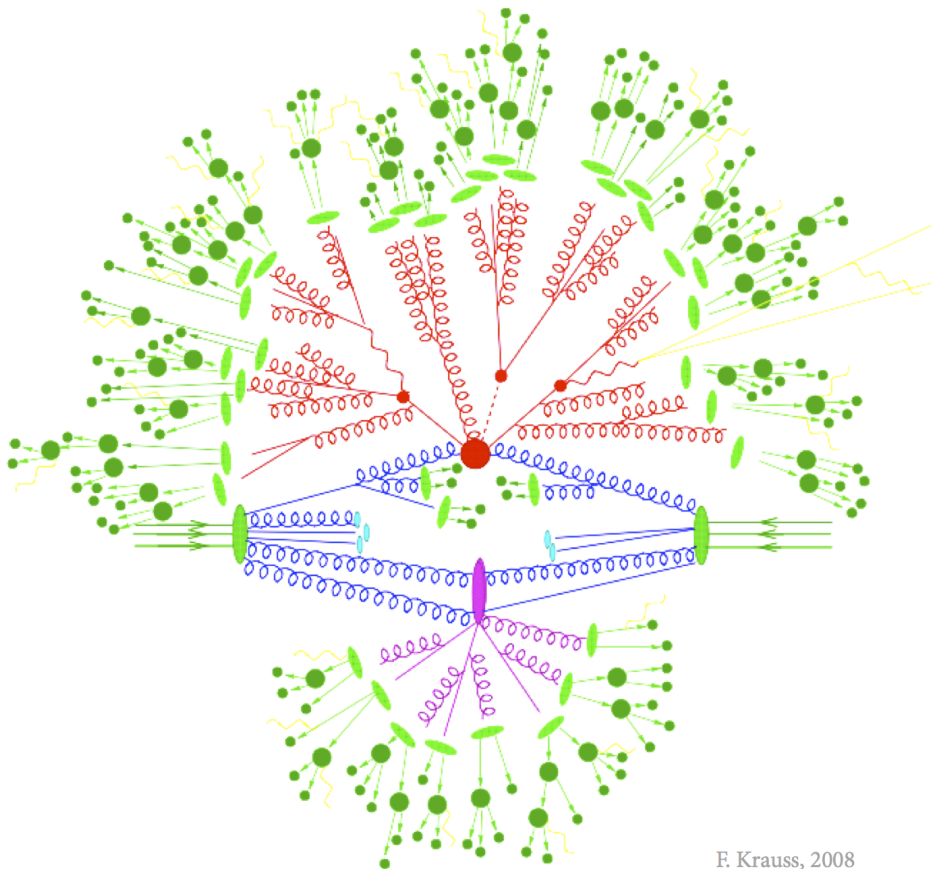
In the **VBF** Higgs to invisible analysis **MET** calculated without including muons is used in the offline analysis and trigger. This choice allows to investigate the irreducible background of $Z \rightarrow \nu\nu$ by using $Z \rightarrow \mu\mu$ as a proxy. Muons are vetoes in the signal region and required in the control regions to recover the usual **MET** value.

3.9 Monte Carlo Simulation

Monte Carlo (MC) methods are a class of computer algorithms that rely on random sampling to obtain numerical results. This type of methods are especially useful in problems with many coupled degrees of freedom where it is difficult to perform analytical

calculations. In particle physics these methods are often used to simulate physics processes, their interaction with detectors and the obtained response.

To simulate one event in the CMS experiment we first start by the physics process itself. It can be split into two sub-processes: hard scattering and hadronization. There are many purpose built software programs that will perform each of these steps. An illustration of how the simulation of proton-proton collision is done with MC programs can be found in figure 3.4. A review of the available generators for LHC physics can be found in reference [62].



F. Krauss, 2008

Figure 3.4: Illustration of a proton-proton collision as implemented in some MC event generators [63]. Sub-processes are represented, the hard-scattering in the center of the diagram, the parton showering in red, hadronization in green. We can also observe the UE interaction and its showering in purple.

General purpose particle physics event generators like PYTHIA 8 [64, 65], HERWIG++ [66] and SHERPA [67] are able to do both hard scattering and hadronization steps for a wide variety of physics processes. Typically these programs are restricted to $2 \rightarrow 2$ and $2 \rightarrow 1$ hard processes calculated at **Leading Order (LO)**.

There are many other dedicated matrix-element generators, like MADGRAPH 5 [68], ALPGEN [69] and also SHERPA that focus on the hard process simulation. These programs provide $2 \rightarrow X$ hard scattering where a higher number of partons in the final state is possible. Some generators have also implemented **Next to Leading Order (NLO)** calculations, which provide better kinematics description and lower uncertainties. Two examples of such generators are aMC@NLO [70] and POWHEG [71, 72]. The simulated parton level events then need to be passed to a general purpose event generators for hadronization.

Overlapping of the phase-space description of matrix-element and showering programs needs to be avoided when simulating multi-jets events. This problem rises from software like PYTHIA or HERWIG describing parton radiation as a Markov Chain process based on Sudakov form factors. This approach is only formally correct in the limit of soft and collinear emissions. On the other hand **Matrix Element (ME)** programs like MADGRAPH work well for the hard scattering high energy limit but diverges when the partons become soft or collinear.

There are a few jet-parton matching schemes developed to account for this overlap [73]. Showering can be vetoed and the event reweighed accordingly, like in the CKKW scheme [74–76] or events can be rejected altogether like in the MLM scheme [77]. Depending on the generator used for the showering, different schemes are implemented and care must be taken in the definition of the matching parameters.

Most event generators can be finely tuned so important aspects of the simulation can be adjusted to experimental conditions. As an example, in the **CMS** experiment PYTHIA is used with the Z2 tune, which was produced using measurements made using minimum bias data at the Tevatron and at the **LHC** [78].

After the physics event is simulated, the interaction with the detector and the corresponding electronics response is estimated using a precise model of the experiment. In the **CMS** experiment GEANT 4 [79, 80] software is used for this task which also relies heavily on **MC** methods.

Chapter 4

Search for H(Inv) decays in the VBF channel with CMS prompt data

In this analysis we focus on Higgs boson decays into invisible particles produced in association with two final state quark jets. These jets will have large rapidity separation and high invariant mass. An event selection criteria has been developed to take advantage of this distinct topology, by selecting two jets with **Vector Boson Fusion (VBF)** characteristics and large **Missing Transverse Energy (MET)** in order to separate this signal from other background processes. We have drawn inspiration from the selection criteria proposed in [81].

The main backgrounds for this analysis are from $Z(\nu\nu)$ +jets and $W(\ell\nu)$ +jets, where the the lepton was not reconstructed or properly identified. These backgrounds are estimated from yields in control regions where we select each boson decay into charged leptons together with a dijet with **VBF** characteristics. These yields are extrapolated to the signal region, using conversion factors determined with the help of **Monte Carlo (MC)** simulation. The background from **Quantum Chromodynamics (QCD)** processes is completely estimated from control regions in data since we cannot rely on **MC** simulation due to insufficient statistics for the extrapolation to the signal region. All other minor backgrounds like from $t\bar{t}$, single-top, diboson, and Drell–Yan($\ell\ell$)+jets processes are estimated directly from **MC**.

The observed data yield together with the estimations of the yields for the signal and backgrounds, allow us to perform a single counting experiment and draw limits on the Higgs branching fraction to invisible.

4.1 Event Selection

In this analysis we use the recorded data by a purpose designed trigger that selects events with at least one dijet with **VBF** characteristics and **MET**. The dijet is required to have its jets in opposite sides of the detector and pass $p_T^{jet_1}, p_T^{jet_2} > 40 \text{ GeV}$, $\Delta\eta > 3.5$ and $M_{jj} > 800 \text{ GeV}$. By requiring any dijet instead of the leading dijet we avoid rejecting events where a **Pile-Up (PU)** jet is a leading jet or the effects of the lower energy resolution of the trigger versus offline. We also require $MET_{no-\mu} > 65 \text{ GeV}$, the use of **MET** without muons allows us to record with the same trigger, a control sample of processes $W(\mu\nu)+\text{jets}$ and $Z(\mu\mu)+\text{jets}$. The **MC** simulated events are re-weighted according to the probability of passing the trigger. The trigger weights are determined in a dataset of event recorded with trigger condition requiring a single muon. They are a function of the offline measurements of sub-leading jet p_T , M_{jj} and $MET_{no-\mu}$.

The signal region is defined by selecting events with a tighter version of the trigger conditions with additional cuts and vetoes. Building on the trigger requirements we select events where the leading pair of particle flow anti- $k_T^{\Delta R=0.5}$ jets have $p_T^{jet_1}, p_T^{jet_2} > 50 \text{ GeV}$, $|\eta| < 4.7$, $\eta_{jet_1} \cdot \eta_{jet_2} < 0$, $\Delta\eta_{jj} > 4.2$, $M_{jj} > 1100 \text{ GeV}$ and large missing energy of at least 130 GeV . We veto events with identified veto electrons or loose muons, as defined in chapter 3, to suppress processes with Z or W boson decays. To reduce **QCD** multi-jet backgrounds we additionally request the selected dijet to pass $\Delta\phi < 1.0 \text{ rad}$, since typically **QCD** jets will be back to back and therefore will have high values for this variable. Finally, a **Central Jet Veto (CJV)** is applied where no additional jet can be present between the two leading jets with $p_T > 30 \text{ GeV}$.

The event selection was optimized by setting the lepton vetoes to the recommended values by the relevant **Particle Object Group (POG)** and the **Central Jet Veto (CJV)** to a value where its behaviour is well understood. All other thresholds were optimised to obtain the best possible signal significance which was calculated with a profile likelihood method that takes into consideration all relevant systematics. In this calculation the Higgs mass was assumed to be 125 GeV and a branching ratio to invisible of 100% . The variables involved in the trigger (jet p_T , M_{jj} and **MET**) are constrained to be above the 95% efficiency working point of the trigger. Distributions of the selected dijet M_{jj} , $\Delta\eta$, $\Delta\phi$ and of the **CJV** obtained using **MC** simulation are shown on figure 4.1 together with the optimized cut thresholds.

To estimate the signal yields the POWHEG **MC** generator [71, 72] was used to create events with a Higgs boson produced via the **VBF** channel with **Standard Model (SM)**

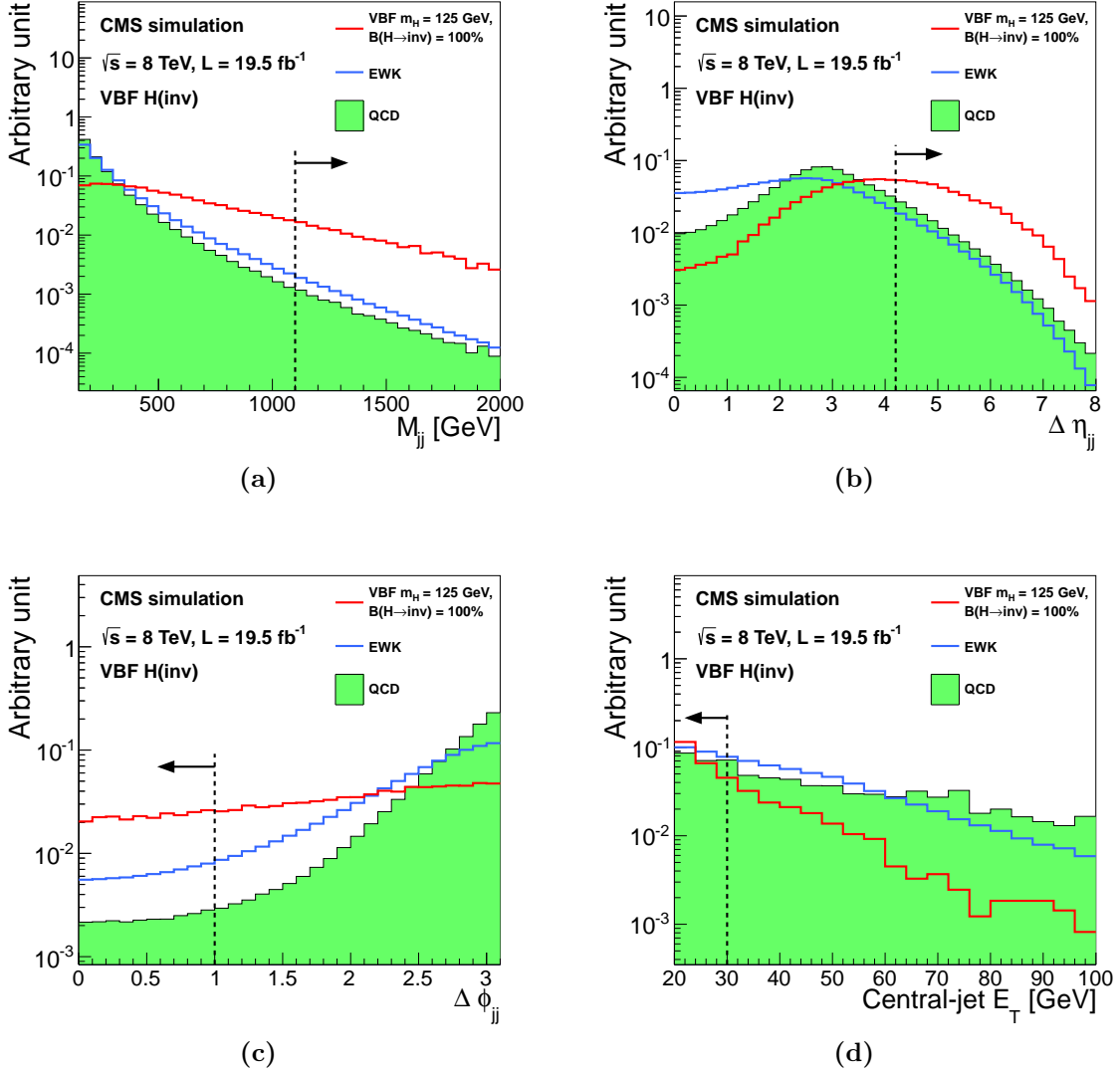


Figure 4.1: Distributions of (a) M_{jj} , (b) $\Delta \eta_{jj}$, (c) $\Delta \phi_{jj}$, (d) and central jet p_T in background and signal MC simulation. The distributions are shown after requiring two jets with $p_T^{jet_1}, p_T^{jet_2} > 50 \text{ GeV}$, $|\eta| < 4.7$, $\eta_{jet1} \cdot \eta_{jet2} < 0$, $M_{jj} > 150 \text{ GeV}$, and $\text{MET} > 130 \text{ GeV}$. The arrows correspond to the thresholds applied for the final selection, after optimization. [82]

couplings and with mass of 125 GeV. The obtained signal efficiency was $(6.8 \pm 0.3) \times 10^{-3}$, which corresponds to an event yield of 210 ± 29 (syst). The signal efficiency dependency on jet p_T , dijet M_{jj} , and **MET** is correlated and of comparable amounts. Additionally, a small amount of gluon-fusion signal, where the **Initial State Radiation (ISR)** emissions take the role of the **VBF** jets, is also expected to pass the signal event selection. Using

the same MC event generator this contribution has been estimated to be of 14 ± 10 (syst) events.

4.2 Background Estimation

The irreducible background $Z(\nu\nu)$ +jets is estimated from data using as proxy $Z(\mu\mu)$ decays. A control region for the Z background is defined with the same event selection as the signal region, with the following changes: instead of the muons veto a pair of opposite charge tight muons is required with an invariant mass compatible with a Z decay of $60 < M_{\mu\mu} < 120$ GeV. We veto the event if any more additional veto electrons or loose muons are present. We use $MET_{no-\mu}$ to emulate the signature from a Z decay into neutrinos. We can extrapolate the number of events in signal region using equation 4.1.

$$N_{\nu\nu}^s = (N_{\mu\mu\text{obs}}^c - N_{\text{bkg}}^c) \cdot \frac{\sigma(Z \rightarrow \nu\nu)}{\sigma(Z/\gamma^* \rightarrow \mu\mu)} \cdot \frac{\varepsilon_{Z\text{MC}}^s}{\varepsilon_{Z\text{MC}}^c}. \quad (4.1)$$

The MCFM MC generator [83] was used to estimate the ratio of cross sections in equation 4.1 as $\sigma(Z \rightarrow \nu\nu)/\sigma(Z/\gamma^* \rightarrow \mu\mu) = 5.651 \pm 0.023$ (syst) for $m_{Z/\gamma^*} > 50$ GeV. The selection efficiency terms are calculated using a DY($\ell\ell$)+jets MC simulation, for the signal region the muons are ignored and the obtained efficiency is $\varepsilon_{Z\text{MC}}^s = (1.65 \pm 0.27)$ (syst)) and $\varepsilon_{Z\text{MC}}^c = (1.11 \pm 0.17)$ (syst)) $\times 10^{-6}$ for the control region. The event yield observed in this control region is of $N_{\mu\mu\text{obs}}^c = 12$ events. The other backgrounds in the control region are estimated using MC simulation of the $t\bar{t}$, diboson and single-top processes being $N_{\text{bkg}}^c = 0.23 \pm 0.15$ (syst) event. Using these results the contribution of the $Z(\nu\nu)$ background in the signal region is estimated as 99 ± 29 (stat) ± 25 (syst) events. Figure 4.2 shows the MET and dijet invariant mass distributions with a less strict Z control region event selection, where $\Delta\eta_{jj}$, $\Delta\phi_{jj}$ and CJV requirements are not enforced and requiring dijet $M_{jj} > 1000$ GeV.

The W boson backgrounds, $W(e\nu)$ +jets and $W(\mu\nu)$ +jets, are estimated in control region that select a single lepton. Two regions are defined following the approach used for the Z boson background. The $W(\mu\nu)$ control region is defined by replacing the *loose muon* veto by a requirement of one *tight muon* and vetoing any event with additional *loose muons*. For this control region the $MET_{no-\mu}$ is used to replicate what would be expected if the

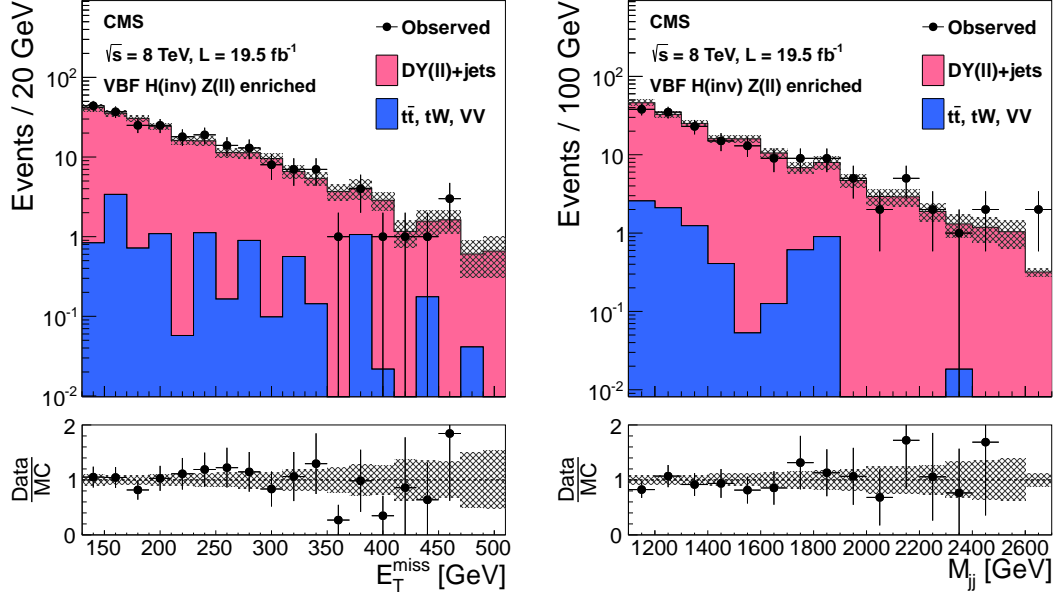


Figure 4.2: Distribution for **MET** on the right and M_{jj} on the left for a relaxed Z control region, with no requirements on $\Delta\eta_{jj}$, $\Delta\phi_{jj}$, or **CJV** and with a $M_{jj} > 1000 \text{ GeV}$ requirement. Backgrounds are shown cumulatively, normalized to data, and with systematic uncertainty shown as a hatched region. The lower panels show the ratio of data to the simulated background. [82]

muon was miss reconstructed or miss identified. The $W(e\nu)$ control region is defined by replacing the *veto electron* veto by a requirement of one *tight electron* and vetoing any event with additional *veto electrons*. For this control region we do not recompute **MET** since it is included in the trigger requirements. Equation 4.2 can be used to extrapolate the events in both this control regions to the signal region.

$$N_\ell^s = (N_{\ell\text{obs}}^c - N_{\text{bkg}}^c) \cdot \frac{N_{\text{WMC}}^s}{N_{\text{WMC}}^c}, \quad (4.2)$$

Where N_{WMC}^s and N_{WMC}^c are the number of event in signal and control regions $W(\ell\nu)+\text{jets}$ obtained from **MC** simulation. These ratios are estimated as $N_{\text{WMC}}^s/N_{\text{WMC}}^c$ is equal to 0.347 ± 0.045 (syst) for $W(\mu\nu)$ and 1.08 ± 0.21 (syst) for $W(e\nu)$. In data the observed yields in the $W(\mu\nu)$ control region is 223 events, with estimated backgrounds from other processes of 30.4 ± 7.0 (syst) events. For the $W(e\nu)$ control region the observed yield is 65 events with estimated backgrounds from other processes of 7.1 ± 4.7 (syst) events.

The extrapolated background in the signal region is 66.8 ± 5.2 (stat) ± 15.7 (syst) events for the $W(\mu\nu)$ background and 62.7 ± 8.7 (stat) ± 18.1 (syst) for the $W(e\nu)$ background.

The $W(\tau\nu)+\text{jets}$ process where the tau decays hadronically τ_{had} is estimated in a similar way to $W(e\nu)+\text{jets}$ and $W(\mu\nu)+\text{jets}$. The $W(\tau_{had}\nu)$ control region is defined like the signal region with the additional requirement of one tau following the description of chapter 3, no other additional lepton are allowed, and the **CJV** is not applied to increase the yield. We estimated the yield in the signal region $N_{\tau_{had}}^s$ using equation 4.2. The conversion factor is derived again from the prediction of the number of events in the signal and control regions for this process from **MC** simulation.

In this control region a yield of 32 events was observed with an **MC** simulation estimated background of 15.2 ± 3.6 (syst), leading to an estimated signal region contribution for the $W(\tau_{had}\nu)$ background of 53 ± 18 (stat) ± 18 (syst) events.

To increase the confidence in the **MC** background model and the extrapolations to the signal regions, we compute the expected data yields from one control regions to another using conversion factors determined from **MC** simulation. For example, the $W(\mu\nu)$ control region date yield is used to compute yield of the the $Z(\mu\mu)$ region is given by using equation 4.3. In all cases, the estimations agreed, within uncertainties, with the observed yields in data.

$$N_{\mu\mu}^c = (N_{\mu\text{obs}}^c - N_{\text{bkg}}^c) \cdot \frac{N_{Z\text{MC}}^c}{N_{W\text{MC}}^c}, \quad (4.3)$$

The **QCD** multijet background is estimated in the signal region by defining four regions depending or passing or failing the **MET** and **CJV** requirements. We define these regions after the full remaining selection as follows:

- A: fail **MET** criteria, fail **CJV** criteria;
- B: pass **MET** criteria, fail **CJV** criteria;
- C: fail **MET** criteria, pass **CJV** criteria;
- D: pass **MET** criteria, pass **CJV** criteria.

We use regions A, B and C to estimate the **QCD** multijet contribution in D. These three regions are first subtracted of the electroweak backgrounds, which are already estimated using other control regions, with event yield estimations from **MC** simulation. The **QCD**

multijet yield in region D is then estimated using $N_D = N_B N_C / N_A$ where N_i is the number of events in region i . This method is based on the assumption that the four regions are uncorrelated, which is tested by comparing the MET distributions below $MET < 130$ GeV of both pass and fail CJV. The maximum observed difference was of 40%, which is assigned as a method systematic. Using this method the contribution to signal region of QCD multijets processes is of 30.9 ± 4.8 (stat) ± 23.0 (syst). To increase the confidence on this method, it was applied to a QCD multijet dominated area by changing the $\Delta\phi_{jj}$ requirement to $\Delta\phi_{jj} > 2.6$ rad. In this region 2551 ± 57 (stat) events were observed, after subtraction of other backgrounds which were estimated from MC simulation. The prediction of this method is of 2959 ± 58 (stat) events, which is compatible with the observation within systematic uncertainties. Furthermore, a cross-check was performed using as variables MET and $\Delta\phi_{jj}$, the obtained predictions is consistent with the main method.

The remaining SM background, for the processes $t\bar{t}$, single-top, VV and DY($\ell\ell$)+jets, in the signal region are estimated directly form MC simulation to be $20.0^{+6.0}_{-8.2}$ (syst) events. Table ?? summarizes all background estimations along with the prediction of the yield for a signal with $m_H = 125$ GeV and $\mathcal{B}(H \rightarrow \text{inv}) = 100\%$. The total expected background yield in the signal region is 332 ± 36 (stat) ± 45 (syst).

Process	Event yields
$Z(\nu\nu)$ +jets	99 ± 29 (stat) ± 25 (syst)
$W(\mu\nu)$ +jets	67 ± 5 (stat) ± 16 (syst)
$W(e\nu)$ +jets	63 ± 9 (stat) ± 18 (syst)
$W(\tau_{had}\nu)$ +jets	53 ± 18 (stat) ± 18 (syst)
QCD multijet	31 ± 5 (stat) ± 23 (syst)
Sum ($t\bar{t}$, single top quark, VV, DY)	20.0 ± 8.2 (syst)
Total background	332 ± 36 (stat) ± 45 (syst)
VBF H(inv.)	210 ± 29 (syst)
ggF H(inv.)	14 ± 10 (syst)
Observed data	390
S/B	70%

Table 4.1: Summary of the estimated number of background and signal events, together with the observed yield, in the VBF search signal region. The signal yield is given for $m_H = 125$ GeV and $\mathcal{B}(H \rightarrow \text{inv}) = 100\%$. [82]

4.3 Sources of uncertainty

The data control event samples for V+jets backgrounds small size translates into a large statistical uncertainty on the estimates in the signal region ranging from 5 – 30%. The systematic uncertainty also associated with this channels is dominated by the MC samples statistical uncertainty when calculating the conversion factors from control to signal regions. Important sources of systematic uncertainty also arise from the effects of the jet and MET energy scale and resolution. These effects are estimate by varying the scales and resolutions within their uncertainty, applying them to the jets and unclustered energy and recalculating the MET. Resulting in a systematic uncertainty of 13% in the signal acceptance, 7-15% in the V+jets background estimates, and 60% uncertainty in the QCD multijet background estimate. As described in the previous section an additional uncertainty of 40% is associated with the QCD multijet estimation, but this background yield is small compared with the total. Muon and electron efficiency uncertainties appear due to the scale factors used to correct MC simulation to data and are small.

For the minor backgrounds which were estimated from MC simulation, the dominating uncertainties come from the used physics process cross sections, which are set according to measurements made by other Compact Muon Solenoid (CMS) collaboration analyses, and the jet/MET scale uncertainties. Theoretical uncertainties on the VBF signal yields result from Parton Distribution Function (PDF) uncertainties, factorization and renormalization scale uncertainties. For the gluon fusion signal the dominating uncertainties arise from MC modelling of ISR and other effects. It is estimated by comparing the estimates from different MC generators and is estimated to be 60%. Gluon fusion represents a small amount of the total signal so this uncertainty only has a modest effect. Table 4.2 summarizes the uncertainties taken into account in relation to signal or total background yields. The combined effect of all uncertainties associated with the backgrounds results in an increase of about 65% in the expected upper limit on the $\mathcal{B}(H \rightarrow \text{inv})$.

4.4 Results and conclusions

As shown in table [82], 390 data events were observed in the signal region, this yield is compatible with the background only prediction. Since no evidence of signal is observed 95% Confidence Level (CL) upper limits on the Higgs boson production cross section times branching fraction are computed. The limit are calculated using the CL_s method

Source	Total background	Signal
Control region statistics	11%	-
MC statistics	11%	4%
Jet/ E_T^{miss} energy scale/resolution	7%	13%
QCD background estimation	4%	-
Lepton efficiency	2%	-
Tau ID efficiency	1%	-
Luminosity	0.2%	2.6%
Cross sections	0.5–1%	-
PDFs	-	5%
Factorization/renormalization scale	-	4%
Gluon fusion signal modelling	-	4%
Total	18%	14%

Table 4.2: Summary of the uncertainties in the total background and signal yields in the **VBF** channel. All uncertainties affect the normalization of the yield, and are quoted as the change in the total background or signal estimate, when each systematic effect is varied according to its uncertainties. The signal uncertainties are given for $m_H = 125$ GeV and $\mathcal{B}(H \rightarrow \text{inv}) = 100\%$. [82]

[84–86] based on asymptotic formulae [87], following the standard **CMS** Higgs boson searches combination technique [88, 89]. Systematic uncertainties are incorporated as nuisance parameters and treated according to the frequentist paradigm [89]. The 95% **CL** limits on the Higgs boson production cross section times invisible branching fraction are also presented normalised to the **SM** production cross section [84, 90], which is denoted as $\xi = \sigma \cdot \mathcal{B}(H \rightarrow \text{inv}) / \sigma_{\text{SM}}$. The choice of the **SM** production cross section is arbitrary, since in the existence of a sizeable invisible cross section width would indicate physics beyond the **SM**, which could mean also modification of the production cross-sections. An alternative choice of model for Higgs boson production would not provide additional information since it essentially would scale the limits.

If **SM** production cross sections and acceptances are assumed, the limits on the invisible branching fraction of the 125 GeV Higgs boson ξ can be interpreted as a limit on the invisible branching fraction.

Figure 4.3 shows on the left plot the observed and median expected 95% **CL** limits on the Higgs boson production cross section times invisible branching fraction, as a function of the Higgs boson mass, for the **VBF** production mode. The right plot shows

the corresponding limit on ξ . Assuming the **SM VBF** production cross section and acceptance, this corresponds to an observed (expected) upper limit on $\mathcal{B}(H \rightarrow \text{inv})$ of 0.65 (0.49) for $m_H = 125 \text{ GeV}$.

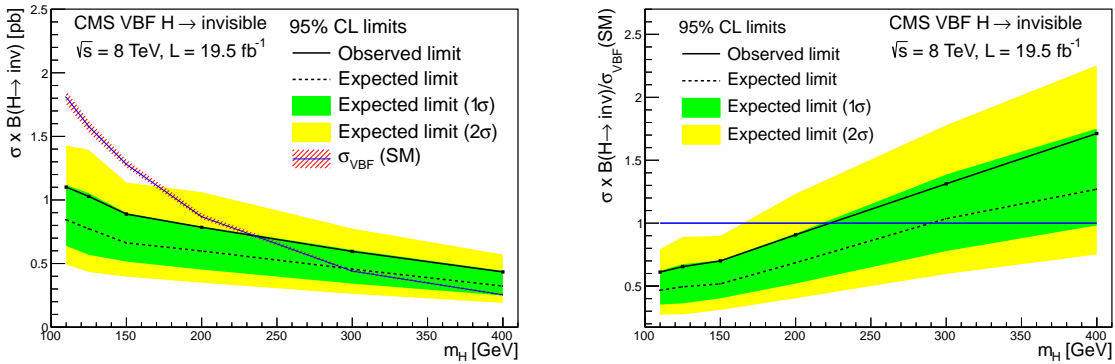


Figure 4.3: Expected and observed 95% CL upper limits on the VBF production cross section times invisible branching fraction (left figure), and normalized to the **SM** Higgs boson **VBF** production cross section (right figure). [82]

Bibliography

- [1] O. S. Bruning, P. Collier, P. Lebrun et al., “LHC Design Report Vol.1: The LHC Main Ring”,,
- [2] L. Evans and P. Bryant, “LHC Machine”, *JINST* **3** (2008) S08001, [doi:10.1088/1748-0221/3/08/S08001](https://doi.org/10.1088/1748-0221/3/08/S08001).
- [3] LEP Injector Study Group Collaboration, “LEP Design Report, Volume 1: The LEP Injector Chain”,,
- [4] P. Mouche, “CERN Document Server: Overall view of the LHC”, <http://cds.cern.ch/record/1708847> (Accessed Dec, 2015).
- [5] ATLAS Collaboration, “The ATLAS Experiment at the CERN Large Hadron Collider”, *Journal of Instrumentation* **3** (2008), no. 08, S08003.
- [6] CMS Collaboration, “The CMS experiment at the CERN LHC”, *Journal of Instrumentation* **3** (2008), no. 08, S08004.
- [7] LHCb Collaboration, “The LHCb Detector at the LHC”, *Journal of Instrumentation* **3** (2008), no. 08, S08005.
- [8] ALICE Collaboration, “The ALICE experiment at the CERN LHC”, *Journal of Instrumentation* **3** (2008), no. 08, S08002.
- [9] C. Lefevre, “The CERN accelerator complex”, <https://cds.cern.ch/record/1260465> (Accessed Dec, 2015).
- [10] CMS Collaboration, “CMS Physics: Technical Design Report Volume 1: Detector Performance and Software”, technical report, Geneva, (2006). There is an error on cover due to a technical problem for some items.
- [11] M. Bajko, F. Bertinelli, N. Catalan Lasheras et al., “Report of the task force on the incident of 19th September 2008 at the LHC”, *LHC Project Report LHC-PROJECT-REPORT-1168* (2009).

- [12] CMS Collaboration, “Multi-year Collisions Plots”,
<https://twiki.cern.ch/twiki/bin/view/CMSPublic/LumiPublicResults> (Accessed Dec, 2015).
- [13] CMS Collaboration, “Average Pileup in 2012”,
<https://twiki.cern.ch/twiki/bin/view/CMSPublic/LumiPublicResults> (Accessed Dec, 2015).
- [14] CMS Collaboration, “CMS Compact Muon Solenoid”,
<http://public.web.cern.ch/public/Objects/LHC/CMSnc.jpg> (Accessed Nov, 2010).
- [15] CMS Collaboration, “CMS, the Compact Muon Solenoid: Technical proposal”,.
- [16] CMS Collaboration, C. Collaboration, “CMS, tracker technical design report”.
1998.
- [17] CMS Collaboration, “Addendum to the CMS tracker TDR”,.
- [18] CMS Collaboration, “The CMS electromagnetic calorimeter project : Technical Design Report”,.
- [19] CMS Collaboration, “Changes to CMS ECAL electronics : addendum to the Technical Design Report”,.
- [20] USCMS, ECAL/HCAL Collaboration, “The CMS barrel calorimeter response to particle beams from 2-GeV/c to 350-GeV/c”, *Eur. Phys. J.* **C60** (2009) 359–373,
[doi:10.1140/epjc/s10052-009-0959-5](https://doi.org/10.1140/epjc/s10052-009-0959-5), [10.1140/epjc/s10052-009-1024-0](https://doi.org/10.1140/epjc/s10052-009-1024-0).
[Erratum: Eur. Phys. J.C61,353(2009)].
- [21] CMS Collaboration, “The CMS hadron calorimeter project : Technical Design Report”,.
- [22] CMS Collaboration, “The CMS magnet project : Technical Design Report”,.
- [23] CMS Collaboration, “The CMS muon project : Technical Design Report”,.
- [24] CMS Collaboration, “Observation of a new boson at a mass of 125 GeV with the CMS experiment at the LHC”, *Phys. Lett.* **B716** (2013) 30–61,
[doi:10.1016/j.physletb.2012.08.021](https://doi.org/10.1016/j.physletb.2012.08.021), [arXiv:1207.7235](https://arxiv.org/abs/1207.7235).
- [25] CMS Collaboration, “CMS The TriDAS Project : Technical Design Report, Volume 2: Data Acquisition and High-Level Trigger”,.

- [26] CMS Collaboration, “CMS TriDAS project : Technical Design Report, Volume 1: The Trigger Systems”,.
- [27] CMS Collaboration Collaboration, “Data Parking and Data Scouting at the CMS Experiment”,.
- [28] CMS Collaboration, “CMS computing: Technical Design Report”. Technical Design Report CMS. CERN, Geneva, 2005. Submitted on 31 May 2005.
- [29] CMS Collaboration, “CMS Technical Design Report for the Level-1 Trigger Upgrade”,.
- [30] CMS Collaboration, “Technical proposal for the upgrade of the CMS detector through 2020”, Technical Report CERN-LHCC-2011-006. LHCC-P-004, CERN, Geneva, (Jun, 2011).
- [31] CMS Collaboration, “The CMS data quality monitoring software: experience and future prospects”, *J. Phys. Conf. Ser.* **513** (2014) 032024, [doi:10.1088/1742-6596/513/3/032024](https://doi.org/10.1088/1742-6596/513/3/032024).
- [32] D. Montgomery and G. Runger, “Applied Statistics and Probability for Engineers”. John Wiley & Sons, 2010.
- [33] W. Adam, B. Mangano, T. Speer et al., “Track Reconstruction in the CMS tracker”, Technical Report CMS-NOTE-2006-041, CERN, Geneva, (Dec, 2006).
- [34] S. Cucciarelli, M. Konecki, D. Kotlinski et al., “Track reconstruction, primary vertex finding and seed generation with the Pixel Detector”, Technical Report CMS-NOTE-2006-026, CERN, Geneva, (Jan, 2006).
- [35] R. Frühwirth, “Application of Kalman filtering to track and vertex fitting”, *Nucl. Instrum. Meth.* **A262** (1987) 444–450, [doi:10.1016/0168-9002\(87\)90887-4](https://doi.org/10.1016/0168-9002(87)90887-4).
- [36] CMS Collaboration, “Measurement of Tracking Efficiency”,.
- [37] K. Rose, “Deterministic Annealing for Clustering, Compression, Classification, Regression, and related Optimization Problems”, *Proceedings of the IEEE* **86** (1998) 2210.
- [38] W. Waltenberger, R. Frühwirth, and P. Vanlaer, “Adaptive vertex fitting”, *Journal of Physics G: Nuclear and Particle Physics* **34** (2007), no. 12, N343.
- [39] CMS Collaboration, “Tracking and Primary Vertex Results in First 7 TeV Collisions”,.

- [40] CMS Collaboration Collaboration, “Commissioning of the Particle-flow Event Reconstruction with the first LHC collisions recorded in the CMS detector”, Technical Report CMS-PAS-PFT-10-001, 2010.
- [41] CMS Collaboration Collaboration, “Particle-Flow Event Reconstruction in CMS and Performance for Jets, Taus, and MET”, Technical Report CMS-PAS-PFT-09-001, CERN, 2009. Geneva, (Apr, 2009).
- [42] CMS Collaboration Collaboration, “Commissioning of the Particle-Flow reconstruction in Minimum-Bias and Jet Events from pp Collisions at 7 TeV”, Technical Report CMS-PAS-PFT-10-002, CERN, Geneva, (2010).
- [43] CMS Collaboration, “Performance of Electron Reconstruction and Selection with the CMS Detector in Proton-Proton Collisions at $\sqrt{s} = 8$ TeV”, *JINST* **10** (2015), no. 06, P06005, [doi:10.1088/1748-0221/10/06/P06005](https://doi.org/10.1088/1748-0221/10/06/P06005), [arXiv:1502.02701](https://arxiv.org/abs/1502.02701).
- [44] T. C. collaboration, “Performance of CMS muon reconstruction in pp collision events at $\sqrt{s}= 7$ TeV”, *Journal of Instrumentation* **7** (2012), no. 10, P10002.
- [45] S. Baffioni, C. Charlot, F. Ferri et al., “Electron reconstruction in CMS”, Technical Report CMS-NOTE-2006-040, CERN, Geneva, (Feb, 2006).
- [46] E. Meschi, T. Monteiro, C. Seez et al., “Electron Reconstruction in the CMS Electromagnetic Calorimeter”, Technical Report CMS-NOTE-2001-034, CERN, Geneva, (Jun, 2001).
- [47] W. Adam, R. Frühwirth, A. Strandlie et al., “Reconstruction of electrons with the Gaussian-sum filter in the CMS tracker at the LHC”, *Journal of Physics G: Nuclear and Particle Physics* **31** (2005), no. 9, N9.
- [48] CMS Collaboration, “Electron Reconstruction and Identification at $\sqrt{s} = 7$ TeV”.
- [49] C. Collaboration, “Performance of CMS muon reconstruction in cosmic-ray events”, *Journal of Instrumentation* **5** (2010), no. 03, T03022.
- [50] CMS Collaboration, “Performance of muon identification in pp collisions at $\sqrt{s} = 7$ TeV”.
- [51] G. P. Salam, “Towards Jetography”, *Eur. Phys. J.* **C67** (2010) 637–686, [doi:10.1140/epjc/s10052-010-1314-6](https://doi.org/10.1140/epjc/s10052-010-1314-6), [arXiv:0906.1833](https://arxiv.org/abs/0906.1833).

- [52] M. Cacciari, G. P. Salam, and G. Soyez, “The Anti- $k(t)$ jet clustering algorithm”, *JHEP* **04** (2008) 063, [doi:10.1088/1126-6708/2008/04/063](https://doi.org/10.1088/1126-6708/2008/04/063), [arXiv:0802.1189](https://arxiv.org/abs/0802.1189).
- [53] M. Cacciari, G. P. Salam, and G. Soyez, “FastJet User Manual”, *Eur. Phys. J.* **C72** (2012) 1896, [doi:10.1140/epjc/s10052-012-1896-2](https://doi.org/10.1140/epjc/s10052-012-1896-2), [arXiv:1111.6097](https://arxiv.org/abs/1111.6097).
- [54] T. C. collaboration, “Determination of jet energy calibration and transverse momentum resolution in CMS”, *Journal of Instrumentation* **6** (2011), no. 11, P11002.
- [55] M. Cacciari and G. P. Salam, “Pileup subtraction using jet areas”, *Phys. Lett.* **B659** (2008) 119–126, [doi:10.1016/j.physletb.2007.09.077](https://doi.org/10.1016/j.physletb.2007.09.077), [arXiv:0707.1378](https://arxiv.org/abs/0707.1378).
- [56] CDF Collaboration, “The Dijet angular distribution in $p\bar{p}$ collisions at $\sqrt{s} = 1.8$ TeV”, *Phys. Rev. Lett.* **69** (1992) 2896–2900, [doi:10.1103/PhysRevLett.69.2896](https://doi.org/10.1103/PhysRevLett.69.2896).
- [57] Particle Data Group Collaboration, “Review of Particle Physics*”, *Phys. Rev. D* **86** (Jul, 2012) 010001, [doi:10.1103/PhysRevD.86.010001](https://doi.org/10.1103/PhysRevD.86.010001).
- [58] CMS Collaboration, “Performance of tau-lepton reconstruction and identification in CMS”, *JINST* **7** (2012) P01001, [doi:10.1088/1748-0221/7/01/P01001](https://doi.org/10.1088/1748-0221/7/01/P01001), [arXiv:1109.6034](https://arxiv.org/abs/1109.6034).
- [59] CMS Collaboration, “Reconstruction and identification of τ lepton decays to hadrons and ν_τ at CMS”, [arXiv:1510.07488](https://arxiv.org/abs/1510.07488).
- [60] “Performance of Missing Transverse Momentum Reconstruction Algorithms in Proton-Proton Collisions at $\sqrt{s} = 8$ TeV with the CMS Detector”,
- [61] T. C. collaboration, “Missing transverse energy performance of the CMS detector”, *Journal of Instrumentation* **6** (2011), no. 09, P09001.
- [62] A. Buckley et al., “General-purpose event generators for LHC physics”, *Phys. Rept.* **504** (2011) 145–233, [doi:10.1016/j.physrep.2011.03.005](https://doi.org/10.1016/j.physrep.2011.03.005), [arXiv:1101.2599](https://arxiv.org/abs/1101.2599).
- [63] F. Krauss, “Phenomenology at collider experiments”, http://www.ippp.dur.ac.uk/~krauss/Lectures/MonteCarlos/Pheno_5_08.pdf (Accessed May, 2014).

- [64] T. Sjostrand, S. Mrenna, and P. Z. Skands, “PYTHIA 6.4 Physics and Manual”, *JHEP* **05** (2006) 026, [doi:10.1088/1126-6708/2006/05/026](https://doi.org/10.1088/1126-6708/2006/05/026), [arXiv:hep-ph/0603175](https://arxiv.org/abs/hep-ph/0603175).
- [65] T. Sjostrand, S. Mrenna, and P. Z. Skands, “A Brief Introduction to PYTHIA 8.1”, *Comput. Phys. Commun.* **178** (2008) 852–867, [doi:10.1016/j.cpc.2008.01.036](https://doi.org/10.1016/j.cpc.2008.01.036), [arXiv:0710.3820](https://arxiv.org/abs/0710.3820).
- [66] M. Bahr et al., “Herwig++ Physics and Manual”, *Eur. Phys. J.* **C58** (2008) 639–707, [doi:10.1140/epjc/s10052-008-0798-9](https://doi.org/10.1140/epjc/s10052-008-0798-9), [arXiv:0803.0883](https://arxiv.org/abs/0803.0883).
- [67] T. Gleisberg, S. Hoeche, F. Krauss et al., “Event generation with SHERPA 1.1”, *JHEP* **02** (2009) 007, [doi:10.1088/1126-6708/2009/02/007](https://doi.org/10.1088/1126-6708/2009/02/007), [arXiv:0811.4622](https://arxiv.org/abs/0811.4622).
- [68] J. Alwall, M. Herquet, F. Maltoni et al., “MadGraph 5 : Going Beyond”, *JHEP* **06** (2011) 128, [doi:10.1007/JHEP06\(2011\)128](https://doi.org/10.1007/JHEP06(2011)128), [arXiv:1106.0522](https://arxiv.org/abs/1106.0522).
- [69] M. L. Mangano, M. Moretti, F. Piccinini et al., “ALPGEN, a generator for hard multiparton processes in hadronic collisions”, *JHEP* **07** (2003) 001, [doi:10.1088/1126-6708/2003/07/001](https://doi.org/10.1088/1126-6708/2003/07/001), [arXiv:hep-ph/0206293](https://arxiv.org/abs/hep-ph/0206293).
- [70] J. Alwall, R. Frederix, S. Frixione et al., “The automated computation of tree-level and next-to-leading order differential cross sections, and their matching to parton shower simulations”, *JHEP* **07** (2014) 079, [doi:10.1007/JHEP07\(2014\)079](https://doi.org/10.1007/JHEP07(2014)079), [arXiv:1405.0301](https://arxiv.org/abs/1405.0301).
- [71] S. Frixione, P. Nason, and C. Oleari, “Matching NLO QCD computations with Parton Shower simulations: the POWHEG method”, *JHEP* **11** (2007) 070, [doi:10.1088/1126-6708/2007/11/070](https://doi.org/10.1088/1126-6708/2007/11/070), [arXiv:0709.2092](https://arxiv.org/abs/0709.2092).
- [72] S. Alioli, K. Hamilton, P. Nason et al., “Jet pair production in POWHEG”, *JHEP* **04** (2011) 081, [doi:10.1007/JHEP04\(2011\)081](https://doi.org/10.1007/JHEP04(2011)081), [arXiv:1012.3380](https://arxiv.org/abs/1012.3380).
- [73] S. Hoeche, F. Krauss, N. Lavesson et al., “Matching parton showers and matrix elements”, in *HERA and the LHC: A Workshop on the implications of HERA for LHC physics: Proceedings Part A*. 2006. [arXiv:hep-ph/0602031](https://arxiv.org/abs/hep-ph/0602031).
- [74] S. Catani, F. Krauss, R. Kuhn et al., “QCD matrix elements + parton showers”, *JHEP* **11** (2001) 063, [doi:10.1088/1126-6708/2001/11/063](https://doi.org/10.1088/1126-6708/2001/11/063), [arXiv:hep-ph/0109231](https://arxiv.org/abs/hep-ph/0109231).

- [75] F. Krauss, “Matrix elements and parton showers in hadronic interactions”, *JHEP* **08** (2002) 015, [doi:10.1088/1126-6708/2002/08/015](https://doi.org/10.1088/1126-6708/2002/08/015), [arXiv:hep-ph/0205283](https://arxiv.org/abs/hep-ph/0205283).
- [76] S. Mrenna and P. Richardson, “Matching matrix elements and parton showers with HERWIG and PYTHIA”, *JHEP* **05** (2004) 040, [doi:10.1088/1126-6708/2004/05/040](https://doi.org/10.1088/1126-6708/2004/05/040), [arXiv:hep-ph/0312274](https://arxiv.org/abs/hep-ph/0312274).
- [77] M. L. Mangano, M. Moretti, F. Piccinini et al., “Matching matrix elements and shower evolution for top-quark production in hadronic collisions”, *JHEP* **01** (2007) 013, [doi:10.1088/1126-6708/2007/01/013](https://doi.org/10.1088/1126-6708/2007/01/013), [arXiv:hep-ph/0611129](https://arxiv.org/abs/hep-ph/0611129).
- [78] CMS Collaboration, “Measurement of the Underlying Event Activity at the LHC with $\sqrt{s} = 7$ TeV and Comparison with $\sqrt{s} = 0.9$ TeV”, *JHEP* **09** (2011) 109, [doi:10.1007/JHEP09\(2011\)109](https://doi.org/10.1007/JHEP09(2011)109), [arXiv:1107.0330](https://arxiv.org/abs/1107.0330).
- [79] GEANT4 Collaboration, “GEANT4: A Simulation toolkit”, *Nucl. Instrum. Meth.* **A506** (2003) 250–303, [doi:10.1016/S0168-9002\(03\)01368-8](https://doi.org/10.1016/S0168-9002(03)01368-8).
- [80] J. Allison et al., “Geant4 developments and applications”, *IEEE Trans. Nucl. Sci.* **53** (2006) 270, [doi:10.1109/TNS.2006.869826](https://doi.org/10.1109/TNS.2006.869826).
- [81] O. J. P. Eboli and D. Zeppenfeld, “Observing an invisible Higgs boson”, *Phys. Lett.* **B495** (2000) 147–154, [doi:10.1016/S0370-2693\(00\)01213-2](https://doi.org/10.1016/S0370-2693(00)01213-2), [arXiv:hep-ph/0009158](https://arxiv.org/abs/hep-ph/0009158).
- [82] CMS Collaboration, “Search for invisible decays of Higgs bosons in the vector boson fusion and associated ZH production modes”, *Eur. Phys. J.* **C74** (2014) 2980, [doi:10.1140/epjc/s10052-014-2980-6](https://doi.org/10.1140/epjc/s10052-014-2980-6), [arXiv:1404.1344](https://arxiv.org/abs/1404.1344).
- [83] J. M. Campbell and R. K. Ellis, “MCFM for the Tevatron and the LHC”, *Nucl. Phys. Proc. Suppl.* **205** (2010) 10, [doi:10.1016/j.nuclphysbps.2010.08.011](https://doi.org/10.1016/j.nuclphysbps.2010.08.011).
- [84] LHC Higgs Cross Section Working Group, S. Dittmaier, et al., “Handbook of LHC Higgs Cross Sections: 2. Differential Distributions”, CERN Report CERN-2012-002, (2012).
- [85] A. L. Read, “Presentation of search results: the CL_s technique”, *J. Phys. G* **28** (2002) 2693, [doi:10.1088/0954-3899/28/10/313](https://doi.org/10.1088/0954-3899/28/10/313).
- [86] T. Junk, “Confidence level computation for combining searches with small statistics”, *Nucl. Instrum. Meth. A* **434** (1999) 435, [doi:10.1016/S0168-9002\(99\)00498-2](https://doi.org/10.1016/S0168-9002(99)00498-2).

- [87] G. Cowan, K. Cranmer, E. Gross et al., “Asymptotic formulae for likelihood-based tests of new physics”, *Eur. Phys. J. C* **71** (2011) 1,
[doi:10.1140/epjc/s10052-011-1554-0](https://doi.org/10.1140/epjc/s10052-011-1554-0).
- [88] CMS Collaboration, “Observation of a new boson at a mass of 125 GeV with the CMS experiment at the LHC”, *Phys. Lett. B* **716** (2012) 30–61,
[doi:10.1016/j.physletb.2012.08.021](https://doi.org/10.1016/j.physletb.2012.08.021), [arXiv:1207.7235](https://arxiv.org/abs/1207.7235).
- [89] ATLAS and CMS Collaborations, LHC Higgs Combination Group, “Procedure for the LHC Higgs boson search combination in Summer 2011”, Technical Report ATL-PHYS-PUB-2011-11, CMS NOTE 2011/005, (2011).
- [90] LHC Higgs Cross Section Working Group, S. Dittmaier, et al., “Handbook of LHC Higgs Cross Sections: 1. Inclusive Observables”, CERN Report CERN-2011-002, (2011).

List of Figures

1.1	Underground diagram of the Geneva area showing the Large Hadron Collider (LHC) and its experiments location[4].	2
1.2	Diagram of the European Organization for Nuclear Research (CERN) accelerator complex[9].	4
1.3	Cross sections for several processes for collisions of antiproton-proton and proton-proton as a function of the center of mass energy[6].	6
1.4	Cumulative luminosity versus day delivered to CMS during stable beams and for p-p collisions. This is shown for 2010 (green), 2011 (red) and 2012 (blue) data-taking[12].	7
1.5	Mean number of interactions per bunch crossing at the CMS experiment during 2012[13].	7
1.6	Diagram of CMS experiment showing the experiment in an open configuration and highlighting the position of its sub-detector[14].	8
1.7	Schematic cross section of the CMS tracke[6]. Each line represent a detector module. Double lines represent dual surface back-to-back detector modules. The inner tracker components are shown components: Tracker Endcaps (TEC), Tracker Outer Barrel (TOB), Tracker Inner Disks (TID), Tracker Inner Barrel (TIB) and Pixels.	11
1.8	Diagram of the ECAL layout illustrating the positions of its components[6].	12
1.9	Longitudinal view of the CMS detector highlighting the location of the Hadronic Calorimeter (HCAL) components: HCAL Barrel (HB), HCAL Endcap (HE) HCAL Outer (HO) and HCAL Forward (HF)[6].	14
1.10	Diagram of the CMS muon systems. The location of each muon chamber for each subsystem is showed[10].	16
1.11	Diagram of the CMS Data Acquisition (DAQ) system. Data flow is showed as the lines connecting each electronics or computing units[6].	18
1.12	Diagram of the Level 1 Trigger (L1T) system. The arrows indicate data flow and the number of particle candidates at each step is indicate[6].	19

2.1	Monitoring plots produced by the L1T online rates monitoring tool for run 207269 and the Electron-Gamma object category. The automatically selected algorithm was L1_SingleEG22 for this run. On the left histogram the algorithm cross section as a function of instantaneous luminosity is plotted. The red line is the prediction obtained from fitting data from previous runs while the black points are the measurements for this run. On the right histogram the fraction of the measured value over the prediction is showed as a function of the luminosity section.	25
2.2	Monitoring plot produced by the L1TSync tool for L1 single electron/gamma object category, which is automatically monitoring algorithm L1_SingleEG22 for the run 207269. In the plots data points are the calculated trigger cross section as a function of instant luminosity and the line is the reference fit done from previous runs.	27
2.3	Monitoring plot produced by the L1T Beam Pickup for Timing for the eXperiments (BPTX) monitoring tool for CMS run 207269. On the left the BPTX veto efficiency in relation to the LHC fill bunch structure is showed. On the right for the same algorithm 1 – Miss Fire fraction is showed.	28
2.4	Detail of L1T BPTX monitoring tool histogram for veto efficiency during its field test at run 207269. The monitored bit was disabled manually leading to the monitored drop off efficiency.	29
2.5	Graphic showing the results of the determination of T_{crit} as a function of μ_0 and the corresponding fit for each bad cell hypothesis. Results are for an efficiency of 99% and a fake rate of 1%.	32
2.6	Graphic showing the results of μ_0^{\min} as a function of the number of bins and the corresponding fit for each bad cell hypothesis. Results are for an efficiency of 99% with a fake rate of 1%.	33
2.7	Monitoring plot produced by the L1T occupancy monitoring tool for run 207099 while testing Global Calorimeter Trigger (GCT) plot for isolated Electromagnetic (EM) region occupancy in $\eta - \phi$. On the left is the histogram under test which have been integrated for enough luminosity sections for meaningful results. On the right is an histogram where the cells that have passed the test are marked in green and red for the cells that failed. Two cells were found that fail the preformed tests.	34
2.8	Example of the plots produced by the L1T test summary monitor	35

3.1 Primary vertex resolution in the z coordinate and vertex reconstruction efficiency as a function of the number of constituent tracks.	38
3.2 Distributions for the variables $\Delta\eta_{in}$, $\Delta\phi_{in}$, $\sigma_{i\eta i\eta}$ and H/E for simulated electrons and misidentified jets.	42
3.3 Distributions of the particle flow E_T^{miss} in $Z \rightarrow \gamma\gamma$ and $\gamma+\text{jets}$ events in $\sqrt{s} = 8 \text{ TeV}$ data and simulation.	54
3.4 Illustration a proton-proton collision as implemented in MC event generators.	55
4.1 Distributions of (a) M_{jj} , (b) $\Delta\eta_{jj}$, (c) $\Delta\phi_{jj}$, (d) and central jet p_T in background and signal MC simulation. The distributions are shown after requiring two jets with $p_T^{jet1}, p_T^{jet2} > 50 \text{ GeV}$, $ \eta < 4.7$, $\eta_{jet1} \cdot \eta_{jet2} < 0$, $M_{jj} > 150 \text{ GeV}$, and $\text{MET} > 130 \text{ GeV}$. The arrows correspond to the thresholds applied for the final selection, after optimization[82]	59
4.2 Distribution for MET on the right and M_{jj} on the left for a relaxed Z control region, with no requirements on $\Delta\eta_{jj}$, $\Delta\phi_{jj}$, or CJV and with a $M_{jj} > 1000 \text{ GeV}$ requirement. Backgrounds are shown cumulatively, normalized to data, and with systematic uncertainty shown as a hatched region. The lower panels show the ratio of data to the simulated background. [82]	61
4.3 Expected and observed 95% CL upper limits on the VBF production cross section times invisible branching fraction (left figure), and normalized to the SM Higgs boson VBF production cross section (right figure)[82]	66

List of Tables

1.1	LHC parameters relevant for detectors	5
1.2	Parameters of the CMS superconducting solenoid	16
3.1	Details of the CMS Electron-Gamma POG recommendations for a <i>veto electron</i> . Here barrel is defined as $ \eta_{supercluster} \leq 1.479$ and endcap is $1.479 < \eta_{supercluster} < 2.5$	43
3.2	Details of the CMS Electron-Gamma POG recommendations for a <i>tight electron</i> . Here barrel is defined as $ \eta_{supercluster} \leq 1.479$ and endcap is $1.479 < \eta_{supercluster} < 2.5$	44
3.3	Table of the minimum values of <i>full Boosted Decision Tree (BDT) method</i> score for a Particle Flow (PF) jet to be accepted as coming from the Primary Vertex (PV) using a loose working point. Required minimum values have been binned in jet p_T and η	48
3.4	Summary of the hadronic tau decay modes.	50
4.1	Summary of the estimated number of background and signal events, together with the observed yield, in the VBF search signal region. The signal yield is given for $m_H = 125$ GeV and $\mathcal{B}(H \rightarrow \text{inv}) = 100\%$ [82] . . .	63
4.2	Summary of the uncertainties in the total background and signal yields in the VBF channel. All uncertainties affect the normalization of the yield, and are quoted as the change in the total background or signal estimate, when each systematic effect is varied according to its uncertainties. The signal uncertainties are given for $m_H = 125$ GeV and $\mathcal{B}(H \rightarrow \text{inv}) = 100\%$. [82]	65

Acronyms

ALICE A Large Ion Collider Experiment. 3

APD Avalanche photo-diodes. 12

ATLAS A Toroidal LHC ApparatuS. 3

AVF Adaptive Vertex Fitter. 37

BDT Boosted Decision Tree. 48, 52, 79

BPTX Beam Pickup for Timing for the eXperiments. 27–29, 77

BSM Beyond the Standard Model. 3

CERN European Organization for Nuclear Research. 2–4, 20, 76

CJV Central Jet Veto. 58, 60–63, 78

CL Confidence Level. 64, 65

CMS Compact Muon Solenoid. 3, 6–10, 13, 15–18, 20, 22–29, 36–40, 43–48, 53, 55, 56, 64, 65, 76, 77, 79

CPU Central Processing Unit. 19

CSC Cathode Strip Chamber. 17, 45

CTF Combinatorial Track Finder. 36, 41

DA Deterministic Annealing. 37

DAQ Data Acquisition. 18, 22, 23, 76

DCS Detector Control System. 23

DIP Data Interchange Protocol. 26

DOC Detector On Call. 22

DPG Detector Performance Group. 28, 29

DQM Data Quality Monitoring. 22–25

DT Drift Tube. 17, 45

EB ECAL Barrel. 12

ECAL Electromagnetic Calorimeter. 11–15, 39–42, 53

EE ECAL Endcap. 12

EM Electromagnetic. 34, 48, 51, 77

FCT Fundação para a Ciência e a Tecnologia. vi

GCT Global Calorimeter Trigger. 21, 34, 77

GSF Gaussian Sum Filter. 41

GT Global Trigger. 26, 28

HB HCAL Barrel. 13, 14, 76

HCAL Hadronic Calorimeter. 13–15, 39, 40, 53, 76

HE HCAL Endcap. 14, 76

HF HCAL Forward. 14, 15, 76

HLT High Level Trigger. 19, 20, 23, 26

HO HCAL Outer. 14, 76

HPS Hadron Plus Stips. 50, 51

ID Identification. 43, 48

ISR Initial State Radiation. 59, 64

L1T Level 1 Trigger. 13, 18–30, 33–35, 76, 77

LEP Large Electron Positron collider. 2

LHC Large Hadron Collider. 2–11, 18, 20, 26, 28, 37, 38, 55, 56, 76, 77

LHCb Large Hadron Collider beauty. 3

LINAC2 Linear Particle Accelerator 2. 3

LO Leading Order. 55

LS1 Long Shutdown 1. 21

MC Monte Carlo. 31, 32, 36, 54–58, 60–64

ME Matrix Element. 56

MET Missing Transverse Energy. 50, 53, 54, 57–64, 78

MPF Missing Transverse Energy Projection Fraction. 49

NLO Next to Leading Order. 56

OMDS Online Master Database System. 26

ORCON Offline Reconstruction Condition DB ONline. 26

PDF Parton Distribution Function. 64

PF Particle Flow. 39, 40, 46–48, 50–54, 79

POG Particle Object Group. 40, 43, 44, 46, 48, 53, 58, 79

PS Proton Synchrotron. 3

PSB Proton Synchrotron Booster. 3

PU Pile-Up. 7, 20, 40, 43, 45, 48, 49, 52, 58

PV Primary Vertex. 37, 38, 48, 79

QCD Quantum Chromodynamics. 40, 51, 57, 58, 62–64

RF Radio Frequency. 4

RPC Resistive Plate Chamber. 17

SM Standard Model. 4, 15, 58, 63, 65, 66, 78

SPS Super Proton Synchrotron. 3, 6

TEC Tracker Endcaps. 11, 76

TIB Tracker Inner Barrel. 11, 76

TID Tracker Inner Disks. 11, 76

TOB Tracker Outer Barrel. 11, 76

TSG Trigger Studies Group. 28

UE Underlying Event. 49, 55

VBF Vector Boson Fusion. 36, 47, 53, 54, 57–59, 63–66, 78, 79

VPT Vacuum Photo-Triodes. 12

WbM Web base Monitoring. 24